

The velocity dispersion profile of NGC 6388 from resolved-star spectroscopy: no evidence of a central cusp and new constraints on the black hole mass¹

B. Lanzoni², A. Mucciarelli², L. Origlia³, M. Bellazzini³, F.R. Ferraro², E. Valenti⁴, P. Miocchi², E. Dalessandro², C. Pallanca², D. Massari²

² *Dipartimento di Fisica e Astronomia, Università degli Studi di Bologna, Viale Berti Pichat 6/2, I-40127 Bologna, Italy*

³ *INAF- Osservatorio Astronomico di Bologna, Via Ranzani, 1, 40127 Bologna, Italy*

⁴ *European Southern Observatory, Karl-Schwarzschild-Strasse 2, 85748 Garching bei München, Germany*

9 April, 2013

ABSTRACT

By combining high spatial resolution and wide-field spectroscopy performed, respectively, with SINFONI and FLAMES at the ESO/VLT we measured the radial velocities of more than 600 stars in the direction of NGC 6388, a Galactic globular cluster which is suspected to host an intermediate-mass black hole. Approximately 55% of the observed targets turned out to be cluster members. The cluster velocity dispersion has been derived from the radial velocity of individual stars: 52 measurements in the innermost 2'', and 276 stars located between 18'' and 600''. The velocity dispersion profile shows a central value of $\sim 13 \text{ km s}^{-1}$, a flat behavior out to $\sim 60''$ and a decreasing trend outwards. The comparison with spherical and isotropic models shows that the observed density and velocity dispersion profiles are inconsistent with the presence of a central black hole more massive than $\sim 2000 M_{\odot}$. These findings are at odds with recent results obtained from integrated light spectra, showing a velocity dispersion profile with a steep central cusp of $23 - 25 \text{ km s}^{-1}$ at $r < 2''$ and suggesting the presence of a black hole with a mass of $\sim 1.7 \times 10^4 M_{\odot}$ (Lützgendorf et al. 2011). We also found some evidence of systemic rotation with amplitude $A_{\text{rot}} \sim 8 \text{ km s}^{-1}$ in the innermost 2'' (0.13 pc), decreasing to $A_{\text{rot}} = 3.2 \text{ km s}^{-1}$ at $18'' < r < 160''$.

Subject headings: Globular clusters: individual (NGC 6388); stars: evolution – black hole physics

1. INTRODUCTION

The confirmation of the existence of intermediate mass ($10^3 - 10^4 M_\odot$) black holes (IMBHs) would have a dramatic impact on a number of open astrophysical problems, ranging from the formation of supermassive BHs and their co-evolution with galaxies, to the origin of ultraluminous X-ray sources in nearby galaxies, up to the detection of gravitational waves (e.g., Gebhardt et al. 2005). However, the evidence gathered so far in support of the existence of IMBHs are inconclusive and controversial (see, e.g., Noyola et al. 2010; Anderson & van der Marel 2010). Galactic globular clusters (GCs) are thought to be the best places where to search for these elusive objects. In fact, the extrapolation of the "Magorrian relation" (Magorrian et al. 1998) down to the IMBH masses naturally leads to the GC mass regime. Moreover, numerical simulations have shown that the cores of GCs are the ideal habitat for the formation of IMBHs (e.g. Portegies Zwart et al. 2004). For these reasons, the recent years have seen an increasing number of works dedicated to the search for IMBHs in GCs, exploiting all observational channels, ranging from the detection of X-ray and radio emission (see Strader et al. 2012; Kirsten & Vlemmings 2012, and references therein), to the detailed study of the cluster structure, especially in terms of the shape of the density and velocity dispersion profiles (e.g., Gebhardt et al. 2000; Gerssen et al. 2002; Lanzoni et al. 2007; Noyola et al. 2010; Anderson & van der Marel 2010; Lützgendorf et al. 2011, hereafter L11). In spite of such an effort, however, no firm conclusions could be drawn to date. This is mainly because of the great difficulties encountered from both the theoretical and the observational points of view. In particular, the expected X-ray and radio emission are still quite uncertain. A power-law density profile $\Sigma_*(r) \propto r^\alpha$ with a slope $\alpha \sim -0.3$ (significantly shallower than the one expected in a post-core collapse system: $\alpha \sim -0.7$) is expected in the innermost cluster regions (e.g. Baumgardt, Makino, & Hut 2005; Miocchi 2007), even though this could be a non-univocal signature of a central IMBH (Vesperini & Trenti 2010). In the presence of an IMBH a steep central cusp is expected also in the velocity dispersion profile (Baumgardt, Makino, & Hut 2005; Miocchi 2007). However, the precise determination of the stellar density and (especially) the velocity dispersion is very challenging in the highly crowded central regions of GCs. In particular, measuring the projected velocity dispersion (σ_P) in GCs has always been a very difficult task. In fact, GCs are close enough for allowing to resolve single stars; hence, the estimate of σ_P from the line broadening of integrated light spectra can be easily falsified by the dominant contribution of a few bright

¹Based on observations collected at the European Southern Observatory, Cerro Paranal, Chile (under proposals 381.D-0329, 073.D-0211 and 073.D-0760). Also based on observations with the NASA/ESA HST (Prop. 19835), obtained at the Space Telescope Science Institute, which is operated by AURA, Inc., under NASA contract NAS5-26555.

objects (e.g., Dubath, Meylan & Mayor 1997). On the other hand their stellar densities (especially in the centre) are so high that the measurement of *individual radial velocities* is very challenging from the observational point of view and it requires very high spatial resolution spectroscopy. For the accurate determination of the internal proper motions, both high spatial resolution imaging and long enough time baselines are needed (e.g. McNamara et al. 2003; Anderson & van der Marel 2010; McNamara et al. 2012). Finally, different methodologies for measuring the velocity dispersion could bring to incompatible results (see the case of ω Centauri discussed in van der Marel & Anderson 2010; Noyola et al. 2010).

This paper is devoted to NGC 6388. Using high spatial resolution ($0.025'' \times 0.027''/\text{pix}$) data acquired with the HST/ACS High Resolution Channel (HRC), we discovered a shallow central cusp ($\alpha = -0.2$) in the inner $1''$ and, from the comparison with King models including a central IMBH (Miocchi 2007), we suggested that a $\sim 6 \times 10^3 M_\odot$ BH could be hidden in the center of this cluster (Lanzoni et al. 2007). However, subsequent investigations, both in the X-ray and in the radio bands, argued against such a conclusion (Nucita et al. 2008; Cseh et al. 2010; Bozzo et al. 2011). The question has been recently re-opened by L11, who used *integrated light spectra* acquired with the FLAMES/ARGUS to derive σ_P from the spectral line broadening: they found an increasing trend toward the cluster centre, up to values of $23 - 25 \text{ km s}^{-1}$, and concluded that this is best fitted by assuming the presence of an IMBH of $(1.7 \pm 0.9) \times 10^4 M_\odot$. Here we derive the velocity dispersion profile of NGC 6388 from the *radial velocities of more than 300 individual stars*. We find no evidence of central cusp in the velocity dispersion and the comparison with theoretical models suggests that this is inconsistent with the presence of an IMBH more massive than $\sim 2000 M_\odot$.

The paper is organized as follows. Observations and data analysis are described in Section 2. Results are presented in Sect. 3 and include the determination of the cluster membership (Sect. 3.1), the study of its systemic rotation (Sect. 3.2) and the measurement of the velocity dispersion profile (Sect. 3.3). Section 4 is devoted to the comparison with previous results and theoretical models. The conclusions are presented and discussed in Sect. 5. Appendix A is dedicated to the discussion of the impact of unresolved background and stellar blends on the determination of radial velocities.

2. OBSERVATIONS AND DATA ANALYSIS

2.1. The SINFONI data set for the cluster central region

In order to acquire spectra of individual stars in the center of NGC 6388 we exploited the high spatial resolution capabilities of SINFONI (Eisenhauer et al. 2003), a near-IR (1.1-

2.45 μm) integral field spectrograph fed by an adaptive optics module and mounted on the YEPUN (VLT-UT4) telescope at the ESO Paranal Observatory. By using the 100 mas plate-scale and the K -band grating (sampling the 1.95-2.45 μm wavelength range), we derived spectra at a resolution $R = 4000$ for ~ 60 stars located in a $3.2'' \times 3.2''$ region centered on the cluster gravity center (as quoted in Lanzoni et al. 2007). The observations have been performed in service mode between April and June 2008 (ESO proposal ID: 381.D-0329(A), PI: Lanzoni), under an average seeing of $\sim 0.8''$ (FWHM). A star of magnitude $R \sim 12$ located $\sim 9''$ from the cluster center has been used as natural guide star for adaptive optics correction, leading to an average Strehl ratio² of $\sim 30\%$. The high level of crowding combined with the small field of view prevented us from estimating the sky background through a dithering technique. Hence, for background subtraction purposes the observations were performed with a target-sky-sky-target sequence, using an empty sky region located $\sim 2'$ North-East from the cluster center. A single target frame is the combination of 10 exposures, each one 20 seconds long. The observations have been repeated until a total exposure time of ~ 2.2 hr on target was reached.

We derived a wavelength calibrated 3D data cube, as well as a reconstructed 2D image, by using the SINFONI pipeline v.2.3.2 (Modigliani et al. 2010). Following the pipeline prescriptions, we first corrected all the target and sky data for darks, flats, geometrical distortions and differential atmospheric refraction. We then subtracted the sky background by using the observations of the sky field, we calibrated in wavelength by using a Th-Ar reference arc lamp, and we finally combined the corrected target frames to build the 3D data cube. In principle this provides a total of 32×64 spectra. In practice, in order to minimize the contamination of the spectrum from the light of neighbouring stars, we made the conservative choice of extracting only the spectrum of the central (and most exposed) spaxel corresponding to the star centroid. To this end we performed the photometric analysis of the reconstructed SINFONI image by using ROMAFOT (Buonanno et al. 1983) and thus determined the position of the source centroids. Then, the HST/ACS-HRC catalogue discussed in Lanzoni et al. (2007) was roto-translated on the SINFONI one. The resulting astrometric solution has an accuracy of less than 0.2 spaxels and provided us with a clear-cut identification of 90% of the SINFONI targets. In the remaining cases (corresponding to a candidate SINFONI target surrounded by a few close, fainter companions), a careful visual inspection of the SINFONI image was necessary to precisely locate the spaxel corresponding to the brighter star. With IRAF we thus extracted the 1D spectrum for a total of 59

²The Strehl ratio one of the main parameters characterizing the image quality of data taken with adaptive optics systems and it corresponds to the amount of light contained in the diffraction-limited core of the point spread function, with respect to the total flux.

spaxels (Figure 1) corresponding to 59 stars in the magnitudes range $13 \lesssim I \lesssim 18$ (Figure 2). The extracted spectra have been cleaned from the telluric absorption lines through the division by a spectrum of a featureless early-type star observed each night with the same instrument setup of the science target. The typical signal-to-noise (S/N) ratio *per pixel* at the wavelength $2.18\mu\text{m}$ ranges from ~ 20 at $I = 18$, to ~ 80 for the brightest sources.

2.2. The FLAMES data set for the cluster external regions

The spectra of individual stars beyond the cluster core have been acquired by using the ESO VLT multi-object spectrograph FLAMES (Pasquini et al. 2002), in the MEDUSA UVES+GIRAFFE combined mode. This provides 132 fibers to observe an equivalent number of targets in one single exposure, over a field of view of $25'$ in diameter. Under proposal 381.D-0329(B) (PI: Lanzoni) four pointings of 2320 s each have been performed in June and July 2008 with the GIRAFFE grating HR21 (which samples the Ca II triplet spectral range at a resolution $R = 16200$) and the UVES setup Red Arm 580, covering the wavelength range $4800\text{\AA} < \lambda < 6800\text{\AA}$ at a resolution $R = 47000$. The targets have been selected from the combined HST/ACS-WFC and ESO/WFI photometric catalog already discussed in Lanzoni et al. (2007) and Dalessandro et al. (2008), considering only isolated objects (with no brighter stars within a circle of $1''$ radius), having $V < 17$ and being located along the canonical evolutionary sequences of the color-magnitude diagram (CMD). About 15 GIRAFFE fibers and 2 UVES fibers in each pointing have been used to sample the sky. A total of 422 and 7 stars were observed with GIRAFFE and UVES, respectively. Additional MEDUSA data have been retrieved from the ESO Archive. These include the spectra of red giant branch stars observed with GIRAFFE gratings HR11 and HR13 under program 073.D-0211 (PI: Carretta), with HR13 under program 073.D-0760 (PI: Catelan), and with UVES Red Arm 580 setup in both cases. While some of these stars are in common with the sample discussed above, 99 objects are new. The FLAMES data set therefore consists of a total of 528 individual star spectra.

All these data have been reduced with the most updated versions of the UVES and GIRAFFE ESO pipelines, including bias subtraction, flat-field correction, wavelength calibration through a reference Th-Ar lamp, rebinning to a constant pixel-step, extraction of the one dimensional spectra and (for the UVES targets only) order merging. The accuracy of the wavelength calibration was checked by measuring several emission sky lines in the available spectral ranges and comparing the observed wavelengths to the rest-frame positions quoted by Osterbrock et al. (1996). The removal of the sky background is particularly crucial for the observations performed with the GIRAFFE setup HR21, since the third com-

ponent ($\lambda = 8662\text{\AA}$) of the Ca II triplet is heavily affected by O₂ emission lines. For targets observed with HR11/HR13 and Red Arm 580 setups, instead, the sky level is only a few percent of the star one (because of the brightness of the targets), introducing only a negligible amount of noise in the stellar spectra. In all cases the sky background has been removed by subtracting from each stellar spectrum a master sky spectrum obtained as the median of the observed sky spectra. Each individual sky spectrum has been inspected by eye in order to check for any possible contamination from close stellar components and a few sky spectra showing absorption lines due to the light of close stars have been discarded. Note that the employed pre-reduction procedure takes into account the fiber to fiber relative transmission, in order to properly scale the intensity of each spectrum to the different fiber response. For the targets observed with HR11 and/or HR13 setups, multiple exposures of the same stars are available. In these cases we added together the sky-subtracted spectra to increase the S/N ratio. The same procedure has been adopted for the UVES targets with multiple exposures. The final S/N per pixel is always larger than 50.

2.3. Stellar radial velocities

The radial velocities (V_r) of the SINFONI targets have been measured from the ¹²C¹⁶O band-heads (see Figure 3) and, occasionally, a few atomic lines. For the FLAMES targets we used several atomic lines, depending on the GIRAFFE setup. In all cases we adopted the Fourier cross-correlation method (Tonry & Davies 1979) as implemented in the *fxcor* IRAF task. The observed spectrum is cross-correlated with a template of known radial velocity and a cross-correlation function (i.e., the probability of correlation as a function of the pixel shift) is computed. Then, this is fitted by using a Gaussian profile and its peak value is derived. Once the spectra are wavelength calibrated, the pixel shift obtained by the Gaussian fit is converted into radial velocity. We employed different reference template spectra according to the adopted spectral configuration and stellar type. Basically, we used suitable synthetic spectra computed in the wavelength range covered by the instrumental setup and convolved with a Gaussian profile to reproduce the spectral resolution of the used gratings. For the SINFONI targets we used synthetic spectra computed with the code described by Origlia, Moorwood & Oliva (1993) and following the same procedure (i.e., model atmospheres, atomic and molecular line list) described in Origlia & Rich (2004). For the FLAMES targets we computed synthetic spectra with the Linux version of the SYNTH code (Sbordone 2005).

Four SINFONI spectra are of low quality. Three of them are among the faintest stars in the *K*-band and their spectra have a very low S/N ratio (< 5), probably because of a

bad response of the corresponding spaxels. The spectrum of the star located at the south edge of the field is unusable as a consequence of the adopted jittering procedure. Hence they have been excluded from the subsequent analysis. After a careful analysis of the effects of unresolved background and blended sources on the determination of the radial velocity (see Appendix A), three additional targets have been removed and the final SINFONI sample consists of 52 stars located between $0.2''$ and $1.9''$ from the cluster center. From the FLAMES spectra we measured the radial velocity of all the analyzed targets, corresponding to a total of 528 stars located at distances ranging between $11''$ and $883''$.

The velocity errors are computed for each star following the prescriptions by Tonry & Davies (1979), which take into account the accuracy in the fit of the peak of the correlation function, the errors due to mismatches between object and template spectra and the effect of the anti-symmetric noise component of the correlation function. The typical uncertainties are of a few km s^{-1} for the SINFONI targets, $0.4 - 0.5 \text{ km s}^{-1}$ for the FLAMES giants, and $1.5 - 2 \text{ km s}^{-1}$ for the FLAMES horizontal branch stars because of the blending between the Ca II lines and the Hydrogen Paschen lines. All radial velocities have been reported in the same heliocentric reference system, by applying the corresponding correction computed with the IRAF task *rvcorrect*. The presence of several targets in common among the different FLAMES datasets allowed to verify possible off-sets in the radial velocity zero point, due to the different spectral configurations and wavelength calibrations. We assumed as reference sample the one observed with the HR21 setup, since it represents more than 70% of the entire dataset. No relevant offset is found when this is compared with the other samples, the average radial velocity differences being smaller than 1 km s^{-1} , with a standard deviation $< 1.5 \text{ km s}^{-1}$. This guarantees a good internal homogeneity of our radial velocity zero point and confirms the reliability of our error estimates.

2.4. Stellar metallicities

With the aim of providing an additional constraint to the cluster membership, we also computed the metallicity of our target stars. Unfortunately, a precise measure for the SINFONI targets is prevented by the low spectral resolution of the available data. We could just derive a rough estimate of the target metallicities from a few Fe, Ca and Na lines, suggesting that, within a large uncertainty (~ 0.2 dex), they are compatible with the cluster mean value ($[\text{Fe}/\text{H}] = -0.44 \pm 0.01$; Carretta et al. 2007). To measure the metallicity of the FLAMES targets different methodologies have been adopted according to the different spectral configurations used. The atmospheric parameters (effective temperature and gravity) have been estimated for each target from the comparison between the star position in the

CMD and theoretical isochrones by Pietrinferni et al. (2006). For the stars observed with gratings HR11 and HR13 and with UVES, we performed a direct estimate of the metallicity from the observed equivalent widths (EWs) of the Fe I lines. Given the target atmospheric parameters and the instrumental spectral resolution, we selected only the Fe I lines predicted to be unblended. EWs were measured by means of DAOSPEC (Stetson & Pancino 2008). Details about the choice of the atomic data and the computation of model atmospheres and chemical abundances are in Mucciarelli et al. (2012). In the case of targets observed with the HR21 grating, with the exception of very cold stars and blue horizontal branch stars (for which the Ca II lines are heavily affected by strong TiO molecular bands and Hydrogen Paschen lines, respectively), the metallicity has been derived from the Ca II lines by following the approach described in Carrera et al. (2007). The metallicity has been measured for a total of 508 stars.

3. RESULTS

3.1. Cluster membership

The radial velocities measured from the FLAMES spectra are plotted as a function of the distance from the cluster center (r) in the top-left panel of Figure 4. Most of the observed stars clearly clump around $V_r \sim 80 \text{ km s}^{-1}$, while the remaining ones show a large spread at lower, mostly negative values. Hence, a selection in V_r has been used as driving criterion to distinguish cluster members from field objects.

As apparent from the bottom panels of Fig. 4, the separation between cluster members and field stars is less clear in terms of metallicity. This is indeed expected, since the field population is constituted by disk giants with $[\text{Fe}/\text{H}]$ ranging between zero and -1.0 (Robin et al. 2003). Hence, to determine the average metallicity of NGC 6388 we selected (280) stars with $50 < V_r < 130 \text{ km s}^{-1}$; in addition, based on the star distribution in the $([\text{Fe}/\text{H}], V_r)$ plane, we excluded the most evident outliers by applying a preliminary cut in metallicity: $-0.7 < [\text{Fe}/\text{H}] < -0.1$ (see the dotted box in the bottom-left panel of Fig. 4). The average value turns out to be $\langle [\text{Fe}/\text{H}] \rangle = -0.40$ with a dispersion of 0.08 dex, in good agreement with Carretta et al. (2007). We then conservatively considered as cluster members only those stars having a metallicity value within 3σ from the mean:³ this yields to

³Note that by estimating the atmospheric parameters from a theoretical isochrone appropriate for NGC 6388 (see Sect. 2.4) we implicitly assumed that all stars belong to the cluster. While this is not necessarily true, the Besancon Galactic Model (Robin et al. 2003) shows that the expected contamination from field stars in the color, magnitude and radial velocity ranges covered by our targets is quite low ($\sim 3.5\%$).

276 stars (54% of the total) with $-0.64 < [\text{Fe}/\text{H}] < -0.16$, which are marked as solid circles in the bottom- and top-left panels of Fig. 4. Their metallicity distribution is compared to that of the entire population (508 objects) in the bottom-right panel of the figure. No significant changes are found for reasonable modifications of the assumed cuts in radial velocity and metallicity. Moreover, no significant impact is expected on the following analysis by the potential inclusion of a few interlopers. The resulting 276 FLAMES cluster members are highlighted as solid circles in Figures 5 and 6 which show, respectively, the cluster map and CMD obtained from the photometric catalog presented in Dalessandro et al. (2008). The radial velocities of SINFONI targets range between 56 and 104 km s⁻¹. By also taking into account their very central radial position ($r < 2''$), we consider all of them as cluster members.

To determine the systemic velocity (V_{sys}) of NGC 6388 we adopted even more conservative limits: out of the 276 cluster members, only (240) stars with $r < 350''$ and $60 \leq V_r \leq 105$ km s⁻¹ were selected (see the solid box in the top-left panel of Fig. 4). The mean value, computed with a Maximum-Likelihood method, turns out to be $V_{\text{sys}} = 82.0 \pm 0.5$ km s⁻¹. Different, but still reasonable, assumptions about the limits in cluster-centric distance and/or radial velocity cuts do not produce any significant change in this result, which is also in agreement with the systemic velocity quoted in the literature for NGC 6388 (see, e.g., Harris 1996 – 2010 version; Casetti-Dinescu et al. 2010). The coordinates, magnitudes and radial velocities (referred to V_{sys}) measured for all (52+276) cluster members are listed in Table 1 (where we also give the metallicities of FLAMES targets). In the rest of the paper, \tilde{V}_r will indicate radial velocities referred to the cluster systemic velocity: $\tilde{V}_r \equiv V_r - V_{\text{sys}}$.

3.2. Systemic rotation

Figure 7 shows \tilde{V}_r as a function of the distance from the cluster center for the 52 SINFONI targets. A bimodality is apparent in this distribution and suggests the presence of systemic rotation. To investigate this possibility, we used the method fully described in Bellazzini et al. (2012, and references therein). We considered a line passing through the cluster center with position angle PA varying between 0° (North direction) and 90° (East

Moreover, adopting an isochrone appropriate for the field contaminating population ($[\text{Fe}/\text{H}]=0$, distance =8 kpc), the resulting metallicities turn out to be only a few 0.1 dex larger. In any case, we stress that the driving selection criterion for cluster membership is the radial velocity, while metallicity is used just to refine the selection, even at the cost of rejecting a few cluster members. Most importantly, we stress that any metallicity selection is unable to introduce kinematical biases in the analysis.

direction), by steps of 15° . For each value of PA, such a line splits the SINFONI sample in two. The difference $\Delta\langle\tilde{V}_r\rangle$ between the mean radial velocity of the two sub-samples was computed and it is plotted as function of PA in the upper panel of Figure 8. Its coherent sinusoidal behavior is a signature of rotation and the parameters of the best-fit sine function provide us with the position angle of the rotation axis ($\text{PA}_0 = 11^\circ$) and the amplitude of the rotation curve ($A_{\text{rot}} = 8.5 \text{ km s}^{-1}$; for the exact meaning of this parameter see the discussion in Bellazzini et al. 2012). The corresponding rotation curve is shown in the lower-left panel of Fig. 8. The Kolmogorov-Smirnov probability that the distributions of \tilde{V}_r for the two sub-samples on each side of the rotation axis are drawn from the same parent population is $\sim 4\%$ (lower-right panel), indicating a not particularly high statistical significance, possibly due to the limited sample. We verified that taking into account or ignoring such a rotation has only very weak effects on the computation of the cluster velocity dispersion, which is dominant. While a rotation or shearing signature within $\sim 3''$ from the centre is claimed also by L11, it seems to be mainly caused by the shot noise produced by three bright stars in the field of view (see their Figure 7). In any case, our best-fit position angle of the rotation axis seems not to coincide with their.

We performed a similar analysis also for the FLAMES sample, considering various distance intervals from the cluster centre. The strongest signal of systemic rotation is found for stars with $18'' < r < 160''$ (160 in total). The corresponding parameters are $\text{PA}_0 = 200^\circ$ and $A_{\text{rot}} = 3.2 \text{ km s}^{-1}$, and the Kolmogorov-Smirnov probability for a common origin of the \tilde{V}_r distributions for the two sub-samples is of only 0.6% (see Figure 9). No evidence of significant rotation is instead detected in the outermost cluster regions, where the second moment of the velocity distribution decreases and it becomes increasingly difficult to measure independently the ordered and the random motions. These results do not confirm those recently published by Bellazzini et al. (2012), who suggest that some rotation is present between $\sim 160''$ and $400''$ from the center, based, however, on a small sample of less than 40 stars (in the same radial range we count, instead, more than 100 stars).

We finally emphasize that the results presented in L11 are all in terms of the second moment of the velocity distribution ($V_{\text{RMS}} = \sqrt{V_{\text{rot}}^2 + \sigma_P^2}$, with V_{rot} indicating the rotational velocity). Hence, a direct comparison with their work (Sect. 4.1) requires to analyze the same quantity. Also for this reason, exactly as in L11, we do not apply any correction for rotation and we deal with the second moment of the velocity distribution. However, because the rotation is small, in the following we continue to discuss in terms of velocity dispersion and we use symbol σ_P instead of V_{RMS} all over the paper.

3.3. Velocity dispersion

The radial distribution of \tilde{V}_r for all the selected cluster members is shown in Figure 10. To compute the projected velocity dispersion profile $\sigma_P(r)$, the surveyed area has been divided in a set of concentric annuli, chosen as a compromise between a good radial sampling and a statistically significant number ($\gtrsim 50$) of stars. In each radial bin, σ_P has been computed from the dispersion of the values of \tilde{V}_r measured for all the stars in the annulus, by following the Maximum Likelihood method described in Walker et al. (2006, see also Martin et al. 2007; Sollima et al. 2009). An iterative 3σ clipping algorithm was applied in each bin (the stars thus excluded from the computation are marked as grey circles in Fig. 10). The error estimate is performed by following Pryor & Meylan (1993). The resulting velocity dispersion profile is shown in Figure 11 and listed in Table 2. Given the number of stars in the SINFONI data set (52 objects in total) we computed $\sigma_P(r)$ by considering both one single central bin (solid square in the figure) and two separate annuli (26 stars at $r < 1.2''$, 26 stars beyond; see the empty squares). For the external data set we tried different sets of radial bins (grey region in Fig. 11) and the values obtained by adopting the four annuli listed in Table 2 are shown as black circles. These results show that the velocity dispersion of NGC 6388 has a central ($r \sim 1''$) value of $\sim 13 \text{ km s}^{-1}$, stays approximately flat out to $r \sim 60''$, and then decreases to $\sim 7 \text{ km s}^{-1}$ at $200'' < r < 600''$. If no σ clipping algorithm is applied, the velocity dispersion profile remains almost unchanged, with the only exception of the outermost data-point that rises to $\sim 8.9 \pm 0.8 \text{ km s}^{-1}$.

4. DISCUSSION

4.1. Comparison with previous studies

The inner part ($r < 10''$) of the velocity dispersion profile derived by L11 from the line broadening of integrated-light spectra (triangles in Fig. 11) is clearly incompatible with the one obtained in this study from the radial velocities of individual stars (squares). While the exact reason for such a disagreement is not completely clear, a detailed comparison between our radial velocity measurements and L11 radial velocity map (which is available in electronic form and shown in their Figure 7) suggests that the shot noise corrections applied by these authors may have been insufficient.

Figure 12 approximately reproduces the central $2'' \times 2''$ region of L11’s Figure 7, with the values of V_r that we measured for each individual star in the same field of view marked in black. In the second annulus, for instance, we measure radial velocities as low as 73, 75, 77 km s^{-1} in regions where they quote $V_r > 98 \text{ km s}^{-1}$ (see the red spaxels on the right-hand side).

We also find $V_r = 88, 99 \text{ km s}^{-1}$ where they measure $V_r < 74 \text{ km s}^{-1}$ (cyan region on the upper-left side). This might be because those spaxels in L11 are still highly contaminated, respectively, by the very bright stars with $V_r > 100 \text{ km s}^{-1}$ and $V_r \sim 62 \text{ km s}^{-1}$ (in both studies) that produce the large red spot on the right-hand side of the figure and the dark-cyan spot at the top, despite the applied shot noise correction (see the white asterisks flagging a few spaxels in these red and dark cyan regions). More in general, we note that, even in the case of close stars, our individual radial velocity values can show significant differences, thus indicating that the measurements are independent each other. Instead, the V_r color codes of L11 are quite uniform in several spaxels around the brightest stars (i.e., the degree of correlation, or cross-talking, is high). Even though L11 do not use the values of V_r to measure the cluster velocity dispersion (which is estimated from the line broadening of the combined spectra), this analysis suggests that the spectra of the spaxels close to the brightest stars are still significantly contaminated and provide an artificial broadening of the combined lines. On the other hand, our estimate is directly derived from the dispersion of the radial velocities measured for each individual star in the field of view and the statistics (52 stars) is quite good. Hence we do not see what kind of mistake we could have committed to artificially decrease the value of $\sigma_P(r)$. We finally note that the center adopted by L11 is slightly offset from ours (see Fig. 12).⁴ However, even if we adopt their center and their radial bins, we still find results that are totally inconsistent with a steep central cusp: we measure $\sigma_P = 14.5 \text{ km s}^{-1}$ in the central bin ($r < 0.9''$, 17 stars), $\sigma_P = 12.4 \text{ km s}^{-1}$ in the second annulus ($0.9'' < r < 1.9''$; 27 stars), and $\sigma_P = 13.1 \text{ km s}^{-1}$ if a single bin at $r < 1.3''$ (44 stars) is adopted.

The derived central velocity dispersion also disagrees with the value of $18.9 \pm 0.8 \text{ km s}^{-1}$ determined by Illingworth (1976) and reported by Pryor & Meylan (1993). We believe that, even in this case, the difference comes from the fact that such a value has been obtained from the line broadening of integrated-light spectra, which is prone to shot noise bias. However, we also note that value of 18.9 km s^{-1} refers to the inner $6'' - 12''$ from the centre Illingworth (see Sect.II in 1976), while the effective velocity dispersion quoted by L11 has been computed for $r \leq 40''$. This cast doubts upon the claimed agreement between the value quoted by L11 and that of Illingworth (1976). In addition, the latter author attempted to correct the observed velocity dispersion, thus to derive the central value; the result is quoted in his Table 5: $19.6 \pm 5.7 \text{ km s}^{-1}$. Hence, within such a large uncertainty, both our measurement

⁴Since there is a typo in the coordinates of the cluster centre quoted in equations (2) and (3) of L11, we have used their Figure 6 to approximately locate their centre on the HST/ACS-HRC image. As shown in the left-hand panel of Fig. 12, our centre is located $0.55''$ North and $0.40''$ East from theirs (differently from what is stated in L11).

and that of L11 are formally in agreement with the central velocity dispersion obtained by Illingworth (1976).

4.2. Comparison with models

In this section theoretical models are used to reproduce the observations and derive some constraints on the presence of a central IMBH in NGC 6388. To this end, we follow two different and complementary approaches. First, starting from a family of self-consistent models admitting a central IMBH, we select the one that best reproduces the observed density and velocity dispersion profiles. This provides us with the corresponding structural and kinematical parameters in physical units, including the IMBH mass. Second, we use the observed density profile and include a variable central point mass, to solve the spherical Jeans equation (this is what is done also in L11). We therefore obtain the corresponding family of velocity dispersion profiles, which are then compared to the observations to constrain the BH mass. The first approach is more realistic in terms of the stellar mass-to-light ratio (M/L), since it takes into account various populations of stars with different masses and different radial distributions (as it is indeed expected and observed in mass segregated GCs), while in most applications of the Jeans approach a constant M/L profile is assumed for the computation of the velocity dispersion (but see, e.g., Williams et al. 2009 and Lützgendorf et al. 2012, for Jeans models with varying M/L). Moreover the self-consistent modeling has the advantage that the models stem from a distribution function which is known a priori. Hence, the model consistency (i.e., the non-negativity of the distribution function in the phase-space) is under control and guaranteed by construction. However, the validity of the results is limited to the case in which the assumed models are the correct representation of the true structure and dynamics of the cluster. The second approach is more general, but the resulting models could be non-physical (e.g. Binney & Tremaine 1987). In all cases we assume spherical symmetry and velocity isotropy. These are reasonable assumptions for NGC 6388, which does not show significant ellipticity (Harris 1996) and is thought to be quite dynamically evolved (Ferraro et al. 2012, see also L11).

Self-consistent King and Wilson models – In order to reproduce the observed surface density and velocity dispersion profiles we used self-consistent, multi-mass King (1966) and Wilson (1975) models admitting the presence of a central IMBH (Miocchi 2007).⁵ We assumed the

⁵As detailed in Miocchi (2007), the IMBH is included following the Bahcall & Wolf (1976) phase-space distribution function. These models can be generated and freely downloaded from the Cosmic-Lab web site at the address: <http://www.cosmic-lab.eu/Cosmic-Lab/Products.html>.

same stellar mass spectrum as in Lanzoni et al. (2007), consisting of six mass bins, $0.1M_{\odot}$ wide and ranging between $0.3M_{\odot}$ and $0.9M_{\odot}$, plus a seventh bin containing a population of $1.2M_{\odot}$ white dwarfs, assumed to be the remnants of 4-8 M_{\odot} stars. For the comparison with the observations we used only the density and velocity dispersion profiles of the $[0.8, 0.9] M_{\odot}$ mass group, corresponding to turnoff and giant stars (the ones effectively used in the observations). By following the procedure described in Miocchi (2010), we performed a parametric fit to the observed density profile: this provided us with the model structural parameters (gravitational potential, characteristic radius and ratio between the BH mass and the cluster total mass). Once the projected density is fitted, the shape of the velocity dispersion profile is univocally determined and we therefore applied only a vertical shift (corresponding to a velocity scale factor) to adjust it to the observations. As shown in Figure 13, both the King and the Wilson models properly reproduce the observed profiles.⁶ Once the distance of NGC 6388 is specified (we adopted $d = 13.2$ kpc from Dalessandro et al. 2008), the assumed velocity scale factor univocally determines the value of the cluster total mass (M_{tot}). In turn, given the BH-to-cluster mass ratio set by the density best-fit, this provides us with the mass of the IMBH. The resulting values are listed in Table 3, with $M_{\text{BH}}^{\text{sc}}$ indicating the BH mass obtained from the self-consistent modeling. This approach suggests an IMBH of $\sim 2000M_{\odot}$.

Jeans models – Starting from the best-fit King and Wilson density profiles (upper panels of Fig. 13), we solved the Jeans equation by admitting the presence of an IMBH with a mass (M_{BH}^{J}) ranging between zero and thirty times the best-fit BH mass of the corresponding self-consistent model (i.e., $M_{\text{BH}}^{\text{J}}/M_{\text{BH}}^{\text{sc}} = 0, \dots, 30$, with $M_{\text{BH}}^{\text{sc}} = 2147M_{\odot}$ and $2125M_{\odot}$ for the King and Wilson cases, respectively; see Table 3). Results⁷ are shown in Figure 14 and indicate that our observed velocity dispersion profile is consistent with both the absence of a central IMBH, and the presence of a black hole with a mass up to $\sim 2000M_{\odot}$. Instead we

⁶Just for illustrative purposes, we show in Fig. 10 the $\pm 3\sigma$ velocity dispersion profiles corresponding to the best-fit King and Wilson models (dotted and dashed curves, respectively). As apparent, only a few stars used in the computation of $\sigma_{\text{P}}(r)$ as described in Sect. 3.3 are located below or above these lines, and the velocity dispersion profile that one would obtain by excluding them from the analysis (consistently with the assumption that the stellar system behaves as a perfect King or Wilson model) is still in agreement with the one quoted above.

⁷For fixed BH mass the same velocity dispersion profile is expected in both approaches. However, the comparison between $\sigma_{\text{P}}(r)$ shown in Fig. 13 and the curve corresponding to $M_{\text{BH}}^{\text{J}}/M_{\text{BH}}^{\text{sc}} = 1$ in Fig. 14 reveals a slightly different shape. This is because the profile shown in Fig. 14 corresponds to the velocity dispersion produced by all cluster stars, instead of that produced by the $[0.8, 0.9] M_{\odot}$ mass group only (which is shown in Fig. 13). In fact, the adopted Jeans equation approach is unable to distinguish among different mass groups (or, in other words, it assumes a constant M/L ratio).

find that in order to match the L11 profile an IMBH of $\approx 6 \times 10^4 M_\odot$ should be assumed, in rough agreement with the value quoted by these authors.

The results of our analysis are consistent with both no IMBH and a black hole of no more than $2000 M_\odot$ in the centre of NGC 6388. In particular, its presence is mainly constrained by the cusp of the density profile, while its mass is set by the observed velocity dispersion.⁸ In fact, the steep central increase expected in $\sigma_P(r)$ is not visible in our observations, because, for a $2000 M_\odot$ BH, it is predicted to occur at a very small distance from the centre ($r \lesssim 0.5'' = 0.03$ pc), where we measured only 9 stars. Note that such a small cusp radius is in agreement with the standard computation of the BH sphere of influence ($r_{\text{BH}} \sim GM_{\text{BH}}/\sigma^2$, with σ being the unperturbed velocity dispersion): in fact, assuming $\sigma \sim 14 \text{ km s}^{-1}$, one gets $r_{\text{BH}} \sim 0.7''$. We finally conclude by noticing that the discussed family of self-consistent models are incompatible with the velocity dispersion profile derived by L11 (triangles in Fig. 13). In fact, in these models the velocity dispersion cusp due to the presence of an IMBH always appears within the innermost $3'' - 5''$ from the centre and the main effect of increasing the BH mass is to make the cusp steeper, while there is no mean of moving it outward, at $10''$ or more, where L11 already observed a significant increase of $\sigma_P(r)$.

5. SUMMARY AND CONCLUSIONS

By using the high spatial resolution spectrograph SINFONI, and the multi-object spectrograph FLAMES/MEDUSA installed at the ESO VLT, we measured the radial velocities and metallicities of ~ 600 stars in the direction of the Galactic globular cluster NGC 6388. Based on the measurements of V_r and $[\text{Fe}/\text{H}]$ obtained for the FLAMES sample, we determined the systemic radial velocity and mean metallicity of NGC 6388: $V_{\text{sys}} = 82.0 \pm 0.5 \text{ km s}^{-1}$ and $\langle [\text{Fe}/\text{H}] \rangle = -0.40 \pm 0.08$ (which are in good agreement with the values quoted in the Literature). We also set the criteria for cluster membership: $60 \leq V_r \leq 105 \text{ km s}^{-1}$ and $-0.64 < [\text{Fe}/\text{H}] < -0.16$. This provided us with 52 members located at $0.2 < r < 1.9''$ and 276 between $18''$ and $600''$ from the SINFONI and the FLAMES samples, respectively.

The radial velocities of cluster members were used to study the systemic rotation and

⁸Indeed, the difference in the derived value of M_{BH} with respect to our previous estimate ($5700 M_\odot$) is mostly due to the fact that in Lanzoni et al. (2007) we used a photometric estimate of the cluster total mass under the common assumption of a stellar mass-to-light ratio $M/L_V = 3$ (e.g. Djorgovski 1993). Here, instead, the measured velocity dispersion provides us with a dynamical estimate of the cluster total mass, which turns out to be a factor of ~ 2.2 smaller. This is in agreement with recent results suggesting that $M/L_V \sim 1.3$ in GCs (see, e.g. Sollima et al. 2012).

velocity dispersion of NGC 6388. We found evidence of systemic rotation with amplitude $A_{\text{rot}} \sim 8 \text{ km s}^{-1}$ in the innermost $2''$ (0.13 pc), decreasing to $A_{\text{rot}} = 3.2 \text{ km s}^{-1}$ at $18'' < r < 160''$. In the outermost regions no rotation signature is detected, most probably because the sample is not rich enough and the (largely dominant) velocity dispersion hides the rotation signal. The cluster velocity dispersion profile, both in the very center ($0.2'' < r < 1.9''$) and in the external regions (out to $\sim 600''$) has been derived from the dispersion of *individual star* radial velocities. Results indicate a central value of $\sim 13 - 14 \text{ km s}^{-1}$, a flat behavior out to $\sim 60''$ and a decreasing trend outwards. No evidence of a central cusp in $\sigma_P(r)$ is detected in our data.

These results disagree with those published by L11, who find a steep cusp at $r < 10''$ and a central velocity dispersion of $\sim 23 - 25 \text{ km s}^{-1}$. The reason for such a discrepancy is not completely clear, but it is likely related to the fact that L11 measure σ_P from the line broadening of integrated light spectra. As it is widely discussed in the literature (e.g., Dubath, Meylan & Mayor 1997; Anderson & van der Marel 2010), this procedure is prone to strong biases in the case of Galactic GCs. In fact the acquired spectra can be dominated by the contribution of a few bright stars, instead of effectively sampling the underlying stellar distribution. Certainly, using high-resolution IFU spectroscopy, applying procedures to correct for the shot noise induced by giants, and measuring the line broadening from the combined spectra of several spaxels in the same radial annulus (as it is done in L11) may alleviate the problem. However, (i) the fact that it is hard to imagine methodological errors able to artificially lower the value of $\sigma_P(r)$ if estimated from individual radial velocities (at least if the statistics is good, as it is the case in our study which comprises 52 stars), (ii) the apparently high degree of color correlation among several spaxels close to the brightest stars in the V_r map of L11, and (iii) the disagreement (in terms of both velocity dispersion and radial velocity map; see Figs. 11 and 12) between the two methodologies suggest that measuring σ_P from the integrated light spectra can be fallacious. Indeed, similar discrepancies between the "integrated light" and the "statistical" approaches are found also in the case of ω Centauri, where the latter method is applied to proper motion measurements (see Anderson & van der Marel 2010; Noyola et al. 2010).

The derived velocity dispersion profile is consistent with the presence of an IMBH at most as massive as $\sim 2000 M_\odot$. Given the measured central velocity dispersion ($13-14 \text{ km s}^{-1}$), the derived IMBH mass is in agreement with the expectations of the $M_{\text{BH}} - \sigma$ relation within its quoted uncertainties (see e.g., Gültekin et al. 2009). More sophisticated models are needed to put stronger constraints. However, we believe that to obtain a firm answer it is first necessary to precisely understand why integrated light spectra and the measurement of individual star radial velocities (or proper motions) yield to different values of the velocity dispersion. It is also necessary to collect more data, providing the full

velocity profile (rotation, velocity dispersion, and also the higher order terms; see, e.g., the discussion in Gebhardt et al. 2005). To this end, high spatial resolution photometry and spectroscopy are key observational tools, and new sophisticated methods for the analysis of integral field unit data cubes (e.g., Kamann et al. 2013) are very promising. Meanwhile the James Webb Space Telescope and the planned ground-based extremely large telescopes will become available, for a significant progress in this field of the research it is certainly worth to push even further the usage of the HST and the current generation of spectrometers at 8-10m class telescopes, with integral field capabilities and with adaptive optics.

We warmly thank the referee for the careful reading of the manuscript and the useful suggestions that helped improving the quality of the paper. This research is part of the project COSMIC-LAB funded by the European Research Council (under contract ERC-2010-AdG-267675).

A. IMPACT OF UNRESOLVED BACKGROUND AND BLENDS ON THE DETERMINATION OF V_r

We estimated that the contamination from unresolved background stars (that, in principle, could artificially lower the derived velocity dispersion) is totally negligible. In fact, the dominant contribution to the background is due to unresolved $I \gtrsim 19$ stars which have effective temperatures $T_{\text{eff}} \gtrsim 5500$ K. On the other hand, for $T_{\text{eff}} > 4500$ K the depth of the CO band-heads rapidly decreases for increasing temperature (see Figure 15), and at $T_{\text{eff}} = 5500$ K it is totally negligible with respect to the CO depth at 5000 K (the temperature of our faintest target). We therefore conclude that the unresolved background does not affect the determination of V_r for our targets. We also stress that, even if, we took into account only the brightest targets (45 stars with $I < 16.5$), the resulting central velocity dispersion would remain essentially unchanged: $\sigma_P = 13.8 \pm 1.5 \text{ km s}^{-1}$.

In the case of non-isolated targets, we estimated the effect of blends on the computation of V_r as follows (note that more complete methods have been proposed in the literature, but they are far too much sophisticated for the quality of our data; see, e.g., Kamann et al. 2013). By convolving each star with its point spread function, we estimated the fraction of light from neighbouring objects that contaminates the spaxel of the candidate SINFONI target. We found that the contribution of stars detected in the HST image but not corresponding to a SINFONI centroid was always negligible ($< 5\%$). This is not surprising, since these stars are fainter by at least 1-1.5 magnitudes than the SINFONI targets. Instead, we found seven couples of SINFONI targets where the spaxel corresponding to the fainter star

(and used to measure its V_r ; see Sect. 2.3) was contaminated by 20-25% from the light of the neighbouring (brighter) star. For each of these couples, we simulated the spectrum of the fainter object blended with that of the neighbouring star, by taking into account the percentage of contamination and the differences in flux, temperature and radial velocity between the two “companions”. We then measured the radial velocity from this blended spectrum and we compared it to the input one (i.e., the value previously measured from the observed spectrum of the fainter target). In four cases, the resulting value of V_r was in agreement with the input one within the uncertainties. Discrepancies of about -5 km s^{-1} have been found only for the remaining three cases for which the contaminating (bright) star had V_r smaller than the contaminated (fainter) one. Such a behaviour is due to the asymmetry of the CO band-heads: when the radial velocity of the contaminating star is larger than that of the fainter target, the offset is hidden within the CO band shape, otherwise it is detectable as a shift in V_r towards lower values. We therefore conclude (in agreement with the findings of Kamann et al. 2013) that blending is not a major issue for the measured radial velocities but, to be conservative and to avoid any possible concern about the velocity measurements, we decided to remove the three most affected targets from the sample. Note that including or excluding these stars (or even all the seven targets with larger contamination) has no impact on the derived velocity dispersion.

REFERENCES

- Anderson, J., & van der Marel, R. P. 2010, *ApJ*, 710, 1032
- Baumgardt H., Makino J., Hut P., 2005, *ApJ*, 620, 238
- Bahcall J.N., Wolf R.A, 1976, *ApJ*, 209, 214
- Binney, J., & Tremaine, S. 1987, Princeton, NJ, Princeton University Press, 1987, 747 p.,
- Bellazzini, M., Bragaglia, A., Carretta, E., et al. 2012, *A&A*, 538, A18
- Bozzo, E., Ferrigno, C., Stevens, J., et al. 2011, *A&A*, 535, L1
- Buonanno, R., Buscema, G., Corsi, C. E., Ferraro, I., & Iannicola, G. 1983, *A&A*, 126, 278
- Carrera, R., Gallart, C., Pancino, E., & Zinn, R., 2007, *AJ*, 134, 1298
- Carretta, E., Bragaglia, A., Gratton, R. G., et al. 2007, *A&A*, 464, 967
- Casetti-Dinescu, D. I., Girard, T. M., Korchagin, V. I., van Altena, W. F., & López, C. E. 2010, *AJ*, 140, 1282

- Cseh, D., Kaaret, P., Corbel, S., et al. 2010, MNRAS, 406, 1049
- Eisenhauer, F. et al., 2003, SPIE, 4841, 1548
- Ferraro, F.R. et al., 2012, Nature, 492, 393
- Dalessandro, E., Lanzoni, B., Ferraro, F. R., et al. 2008, ApJ, 677, 1069
- Djorgovski, S. 1993, Structure and Dynamics of Globular Clusters, 50, 373
- Drukier, G.,A., Bailyn, C.D., 2003, ApJ, 597, L125
- Dubath P., Meylan G., & Mayor M., 1997, A&A, 324, 505
- Gebhardt, K., Pryor, C., O’Connell, R. D., Williams, T. B., & Hesser, J. E. 2000, AJ, 119, 1268
- Gebhardt, K., Rich, R. M., & Ho, L. C. 2005, ApJ, 634, 1093
- Gerssen, J., van der Marel, R. P., Gebhardt, K., et al. 2002, AJ, 124, 3270
- Gültekin, K., Richstone, D. O., Gebhardt, K., et al. 2009, ApJ, 698, 198
- Harris, W.E. 1996, AJ, 112, 1487
- Kamann, S., Wisotzki, L., & Roth, M. M. 2013, A&A, 549, A71
- King I.R., 1966, AJ, 71, 64
- Illingworth, G. 1976, ApJ, 204, 73
- Kirsten, F., & Vlemmings, W. H. T. 2012, A&A, 542, A44
- Lanzoni, B., Dalessandro, E., Ferraro, F. R., et al. 2007, ApJ, 668, L139
- Lützgendorf, N., Kissler-Patig, M., Noyola, E., et al. 2011, A&A, 533, A36 (L11)
- Lützgendorf, N., Kissler-Patig, M., Gebhardt, K., et al. 2012, A&A, 542, A129
- Magorrian, J., Tremaine, S., Richstone, D., et al. 1998, AJ, 115, 2285
- Martin, N. F., Ibata, R. A., Chapman, S. C., Irwin, M., & Lewis, G. F. 2007, MNRAS, 380, 281
- McNamara, B. J., Harrison, T. E., & Anderson, J. 2003, ApJ, 595, 187
- McNamara, B. J., Harrison, T. E., Baumgardt, H., & Khalaj, P. 2012, ApJ, 745, 175

- Miocchi, P. 2007, MNRAS, 381, 103
- Miocchi, P. 2010, A&A, 514, A52
- Modigliani, A., Goldoni, P., Royer, F., et al. 2010, Proc. SPIE, 7737,
- Mucciarelli, A., Salaris, M., & Bonifacio, P., 2012, MNRAS, 419, 2195
- Noyola, E., Gebhardt, K., Kissler-Patig, M., et al. 2010, ApJ, 719, L60
- Nucita, A. A., de Paolis, F., Ingrosso, G., Carpano, S., & Guainazzi, M. 2008, A&A, 478, 763
- Origlia, L., Moorwood, A. F. M., Oliva, E., 1993, A&A, 280, 536
- Origlia, L. & Rich, R. M., 2004, AJ, 127, 3422
- Osterbrock, D. E., Fulbright, J. P., Martel, A. R., Keane, M. J., Trager, S. C., & Basri, G., 1996, PASP, 108, 277
- Pasquini, L., et al., 2002, Messenger, 110, 1
- Pietrinferni, A., Cassisi, S., Salaris, M., & Castelli, F. 2006, ApJ, 642, 797
- Portegies Zwart, S. F., Baumgardt, H., Hut, P., Makino, J., & McMillan, S. L. W. 2004, Nature, 428, 724
- Pryor, C., & Meylan, G. 1993, Structure and Dynamics of Globular Clusters, 50, 357
- Robin, A. C., Reyl  , C., Derri  re, S., & Picaud, S. 2003, A&A, 409, 523
- Sbordone, L., 2005, MSAIS, 8, 61
- Sollima, A., Bellazzini, M., Smart, R. L., et al. 2009, MNRAS, 396, 2183
- Sollima, A., Bellazzini, M., & Lee, J.-W. 2012, ApJ, 755, 156
- Stetson, P. B., & Pancino, E., 2008, PASP, 120, 1332
- Strader, J., Chomiuk, L., Maccarone, T. J., et al. 2012, ApJ, 750, L27
- Tonry, J. & Davis, M., 1979, AJ, 84, 1511
- van der Marel, R. P., & Anderson, J. 2010, ApJ, 710, 1063
- Vesperini, E., & Trenti, M. 2010, ApJ, 720, L179

- Walker, M. G., Mateo, M., Olszewski, E. W., et al. 2006, *AJ*, 131, 2114
- Williams, M. J., Bureau, M., & Cappellari, M. 2009, *MNRAS*, 400, 1665
- Wilson, C. P. 1975, *AJ*, 80, 175

id	RA	DEC	B	V	I	\tilde{V}_r	$e_{\tilde{V}_r}$	[Fe/H]	data set
10000131	264.0715464	-44.7349731	–	14.94	12.82	23.5	2.3	–	1
10000216	264.0720428	-44.7353238	–	15.12	12.77	-18.1	2.0	–	1
10000027	264.0712349	-44.7352065	–	15.53	13.80	13.5	2.0	–	1
10000325	264.0724705	-44.7351295	–	15.53	13.78	-18.7	2.7	–	1
...									
30828	264.1096197	-44.7367217	16.90	14.96	–	-4.8	0.3	-0.49	2
7000555	264.0853010	-44.7688900	16.90	15.27	13.40	-13.8	0.2	-0.48	2
7001285	264.0194000	-44.7440720	17.34	15.98	14.37	1.1	0.1	-0.39	2
7001303	264.1128920	-44.7231290	17.74	16.32	14.61	10.0	0.2	-0.41	2

Table 1: Identification number (id), coordinates (in degree), magnitudes in the B , V , and I bands, radial velocity and its uncertainty in km s^{-1} (\tilde{V}_r and $e_{\tilde{V}_r}$, respectively), [Fe/H] abundance, and flag for the data set (fl=1 meaning SINFONI, fl=2 indicating FLAMES) for all the stars selected as cluster members and used to compute the rotational velocity and velocity dispersion of NGC 6388. No values of metallicity are given for the SINFONI targets because of their large uncertainty. The complete version of the table is available online.

r_i	r_e	r_m	N_\star	σ_P	e_{σ_P}
0.2	1.9	1.10	52	13.20	1.33
18.5	86.0	60.17	59	11.90	1.11
86.0	135.0	108.79	70	10.50	0.89
135.0	205.0	165.23	72	9.20	0.77
205.0	609.0	312.75	71	7.00	0.59

Table 2: Velocity dispersion profile of NGC 6388. The three first columns give the internal, external and mean radii (in arcseconds) of each considered radial bin (r_m is computed as the average distance from the centre of all the stars belonging to the bin), N_\star is the number of star in the bin, σ_P and e_{σ_P} are the velocity dispersion and its rms error (in km s^{-1}), respectively.

Model	W_0	r_c	M_{tot}	$M_{\text{BH}}^{\text{sc}}$
King	11	6.4	1.2×10^6	2147
Wilson	11	6.8	1.2×10^6	2125

Table 3: Parameters of the King and Wilson models that best fit the observed surface density and velocity dispersion profiles (see Figure 13). W_0 is a dimensionless parameter proportional to the gravitational potential at the cluster center, r_c is the core radius in arcseconds (defined as the radius at which the projected stellar density drops to half its central value), M_{tot} and $M_{\text{BH}}^{\text{sc}}$ (in units of M_\odot) are, respectively, the total cluster mass and the mass of the central IMBH estimated from the self-consistent modelling approach.

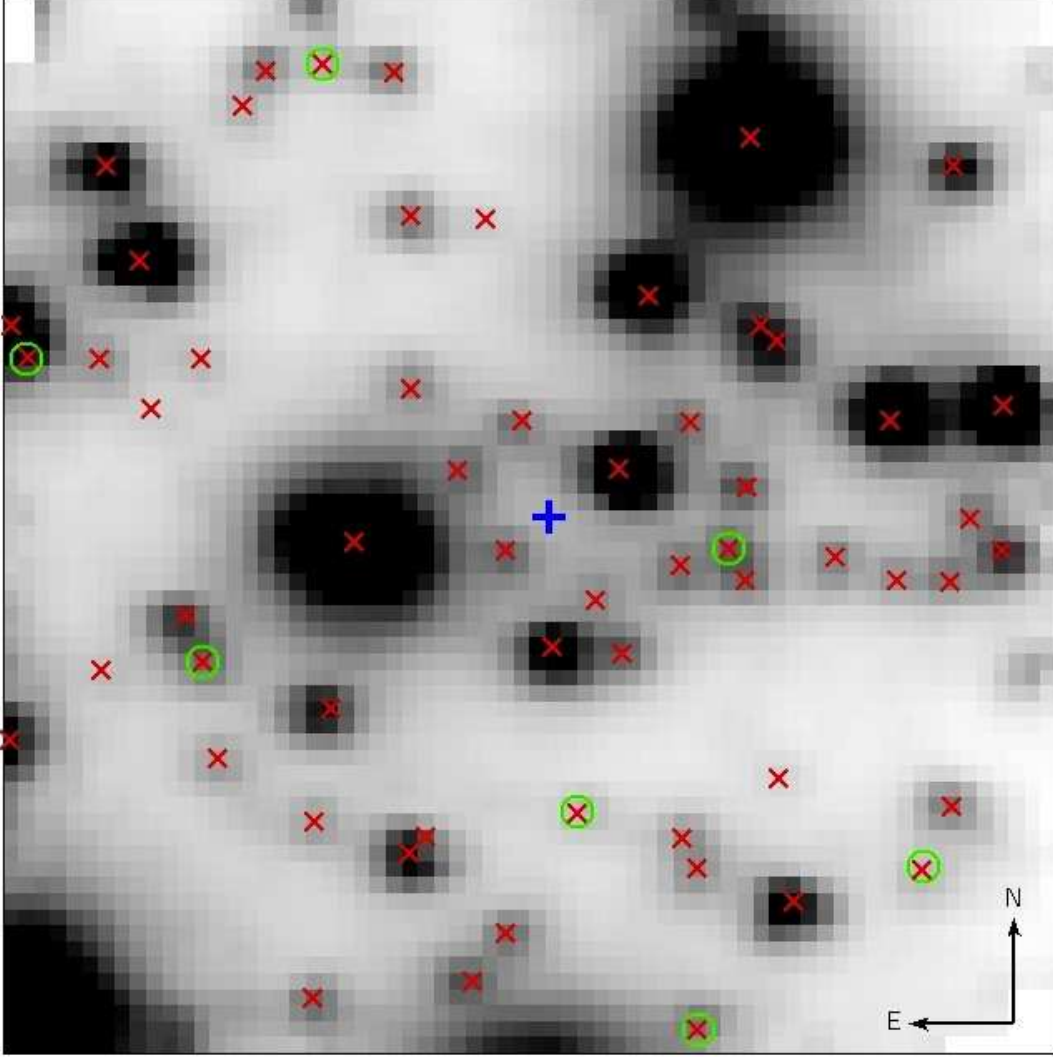


Fig. 1.— Reconstructed SINFONI image. The field of view is $3.2'' \times 3.2''$, North is up, East is left. Red crosses mark the spaxels from which we extracted the spectra, corresponding to stellar centroids measured in the HST/ACS-HRC image. Green circles mark the four stars for which the radial velocity could not be measured and the three targets conservatively rejected because significantly blended with a close brighter star (see Sect. 2.3 and Appendix A). The large blue cross flags the adopted position of the cluster gravity centre (from Lanzoni et al. 2007).

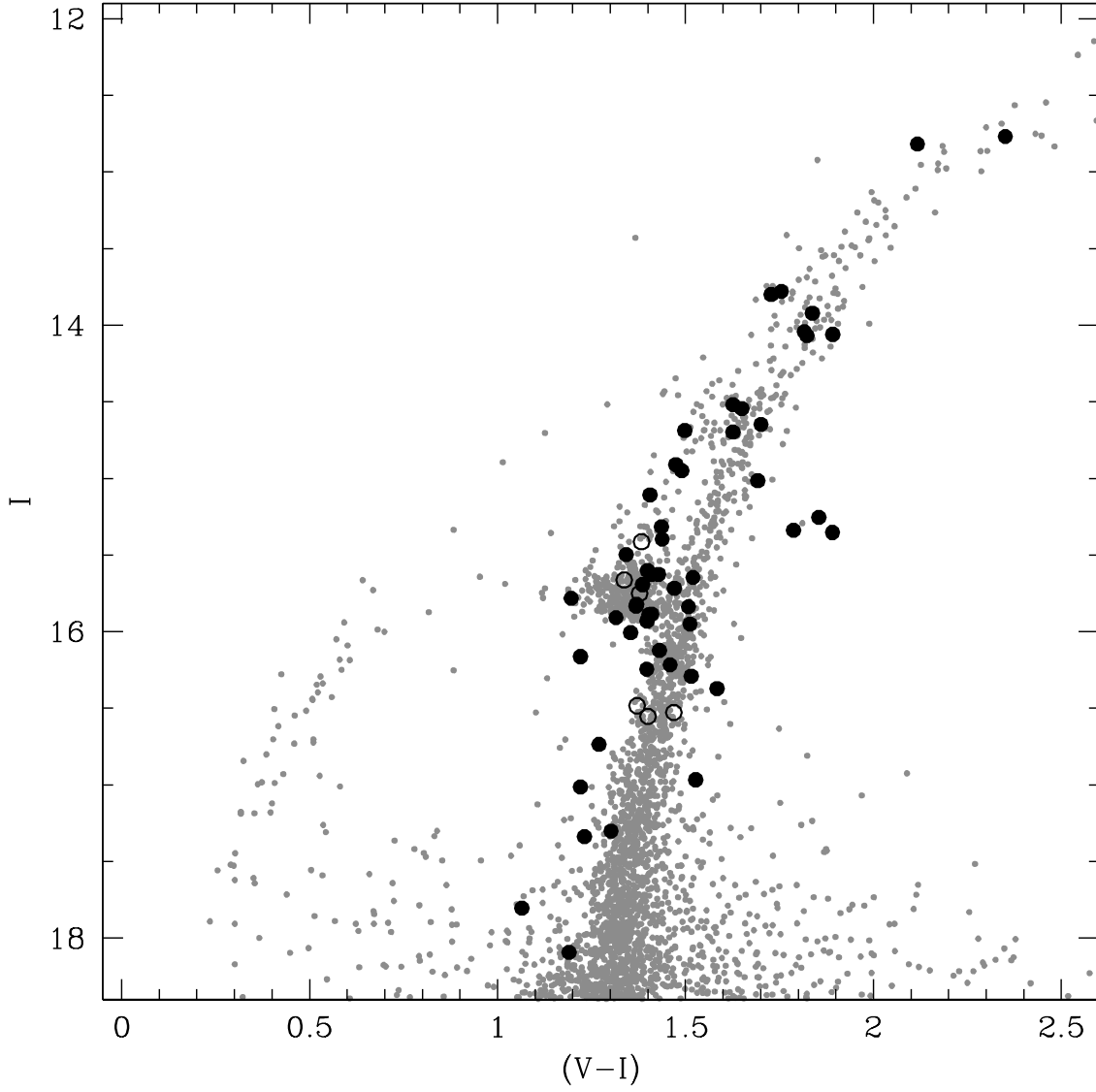


Fig. 2.— HST/ACS-HRC color-magnitude diagram of the central region of NGC 6388. The 59 stars for which we extracted a SINFONI spectrum are highlighted as large circles: solid circles correspond to the 52 objects for which we could reliably measure the radial velocity, empty circles flag the remaining seven stars.

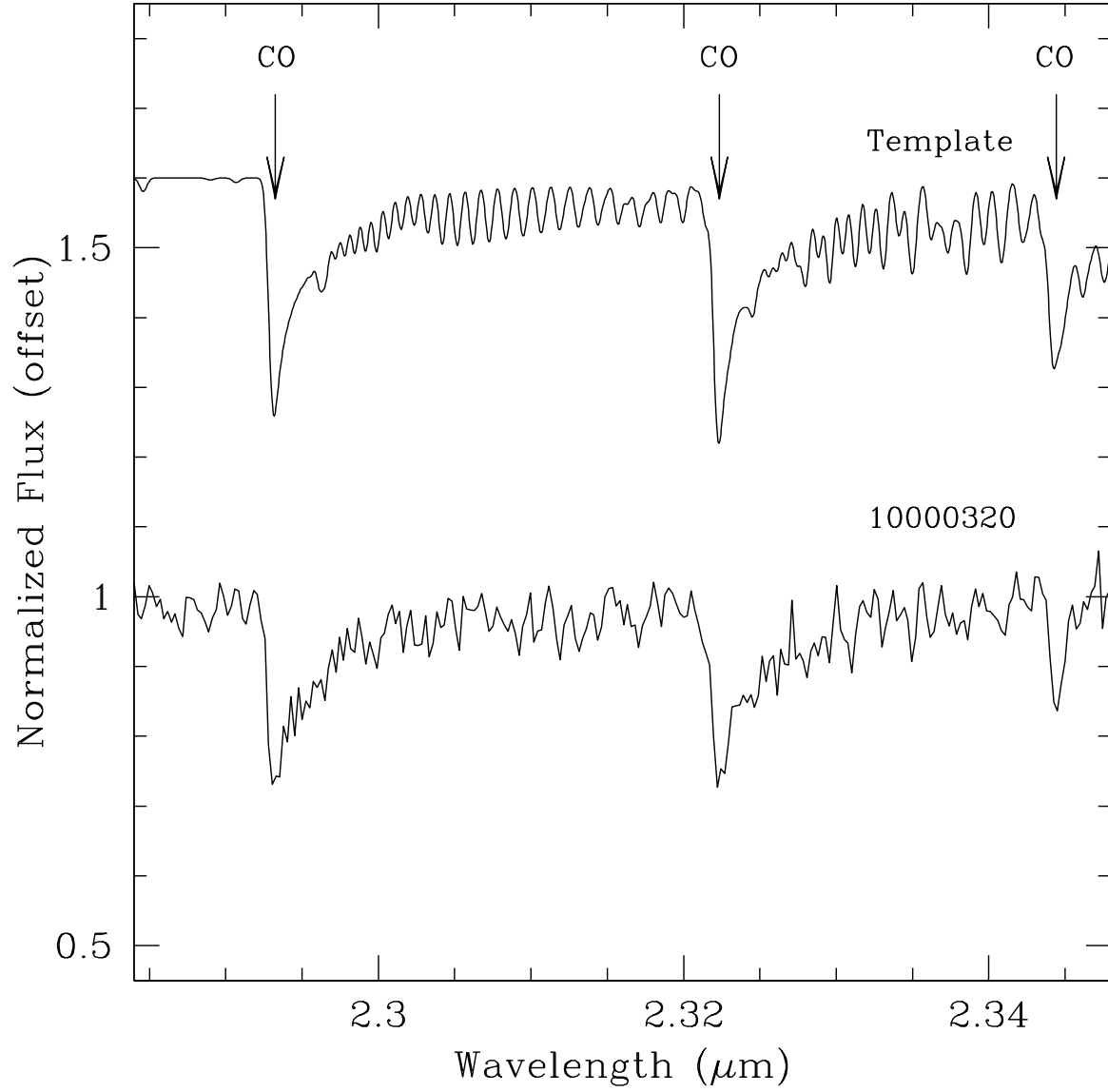


Fig. 3.— Comparison between one spectrum acquired with SINFONI and the appropriate template. Three CO band-heads used to compute the stellar radial velocities are flagged.

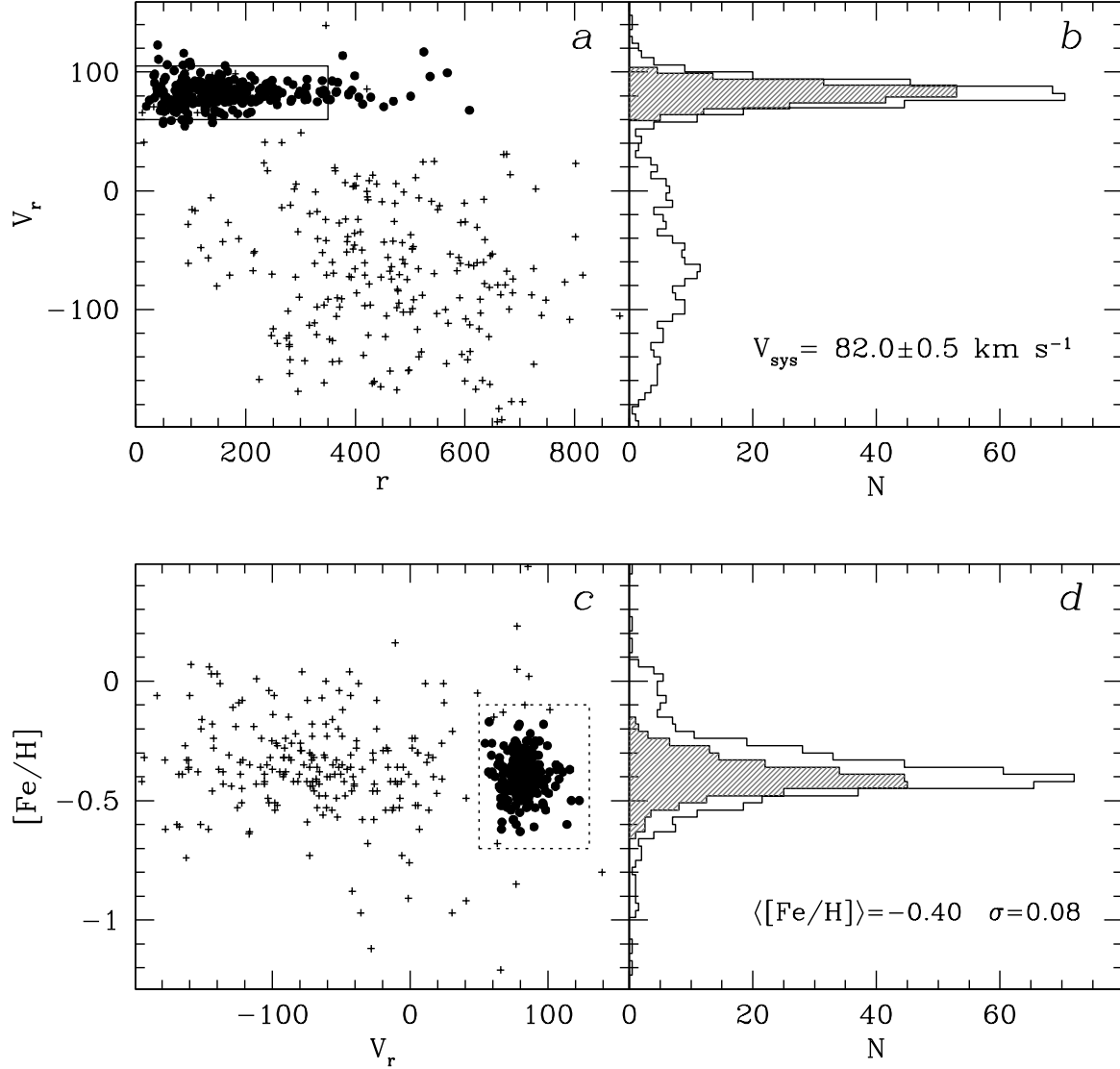


Fig. 4.— Radial velocity and metallicity distributions (top and bottom panels, respectively) of the FLAMES targets used to determine the cluster systemic velocity, mean metallicity and membership. The mean metallicity of NGC 6388 (see label in Panel *d*) has been estimated from the (280) stars enclosed in the dotted box ($50 < V_r < 130 \text{ km s}^{-1}$ and $-0.7 < [Fe/H] < -0.1$) drawn in Panel *c*. Only the (276) stars having a metallicity value within 3σ from the mean have been considered as cluster members (solid circles in Panel *c*). Their metallicity distribution is compared to that of the entire population in Panel *d* (shaded and empty histograms, respectively). The radial velocities of the 276 cluster members (solid circles) are shown as a function of the distance from the cluster centre in Panel *a*. The corresponding number distribution is plotted as shaded histogram and compared to that of the entire FLAMES sample (empty histogram) in Panel *b*. The box drawn in Panel *a* encloses the sub-sample of members used to conservatively compute the cluster systemic radial velocity, which is labelled in Panel *b*.

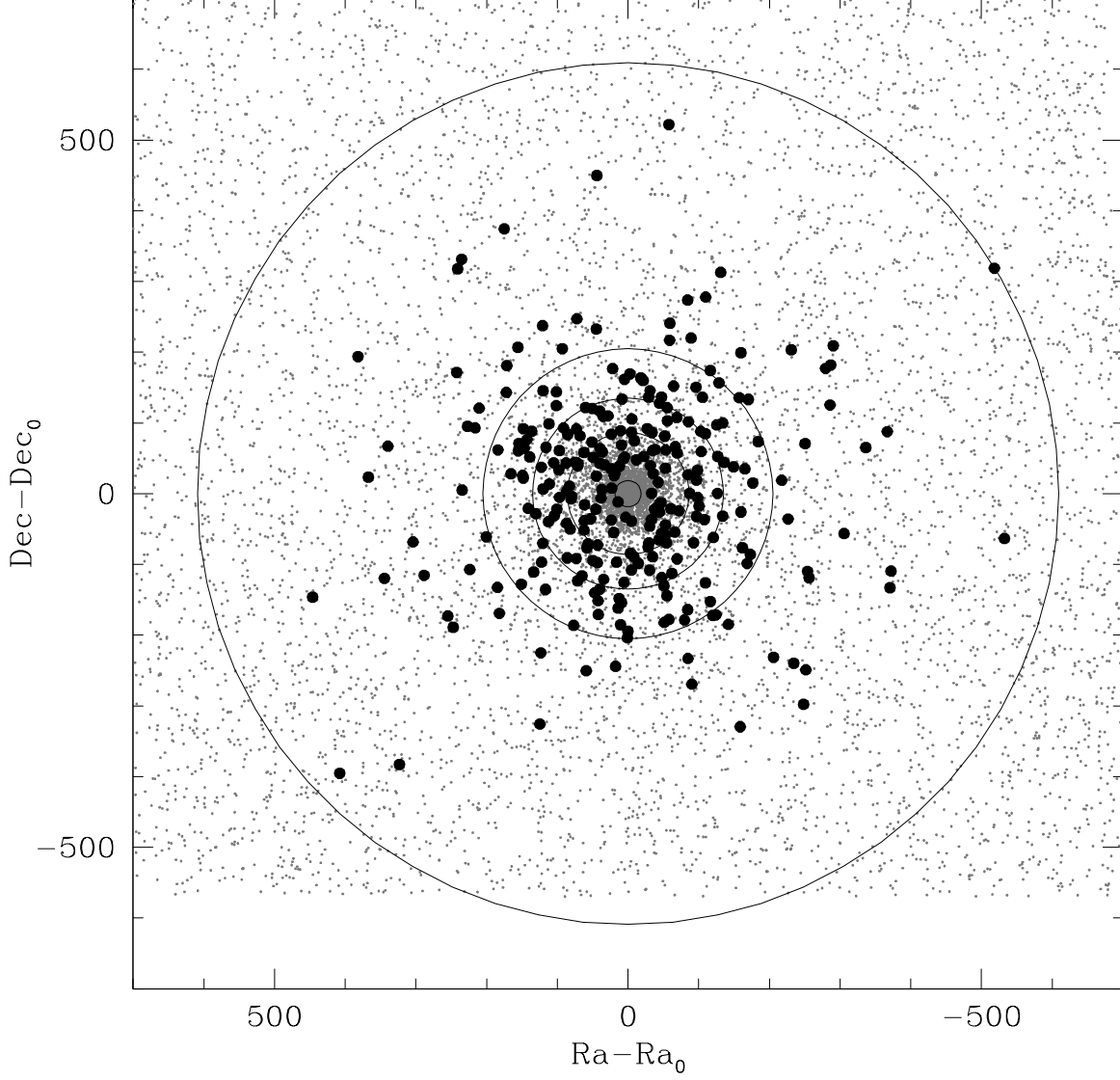


Fig. 5.— Map of stars brighter than $V = 18$, derived from the combined HST/ACS-WFC and ESO/WFI photometric catalog discussed in Dalessandro et al. (2008). The 276 FLAMES targets selected as cluster members are highlighted as large solid circles. The concentric annuli used to compute the cluster velocity dispersion profile in the external regions (see Table 2) are also marked.

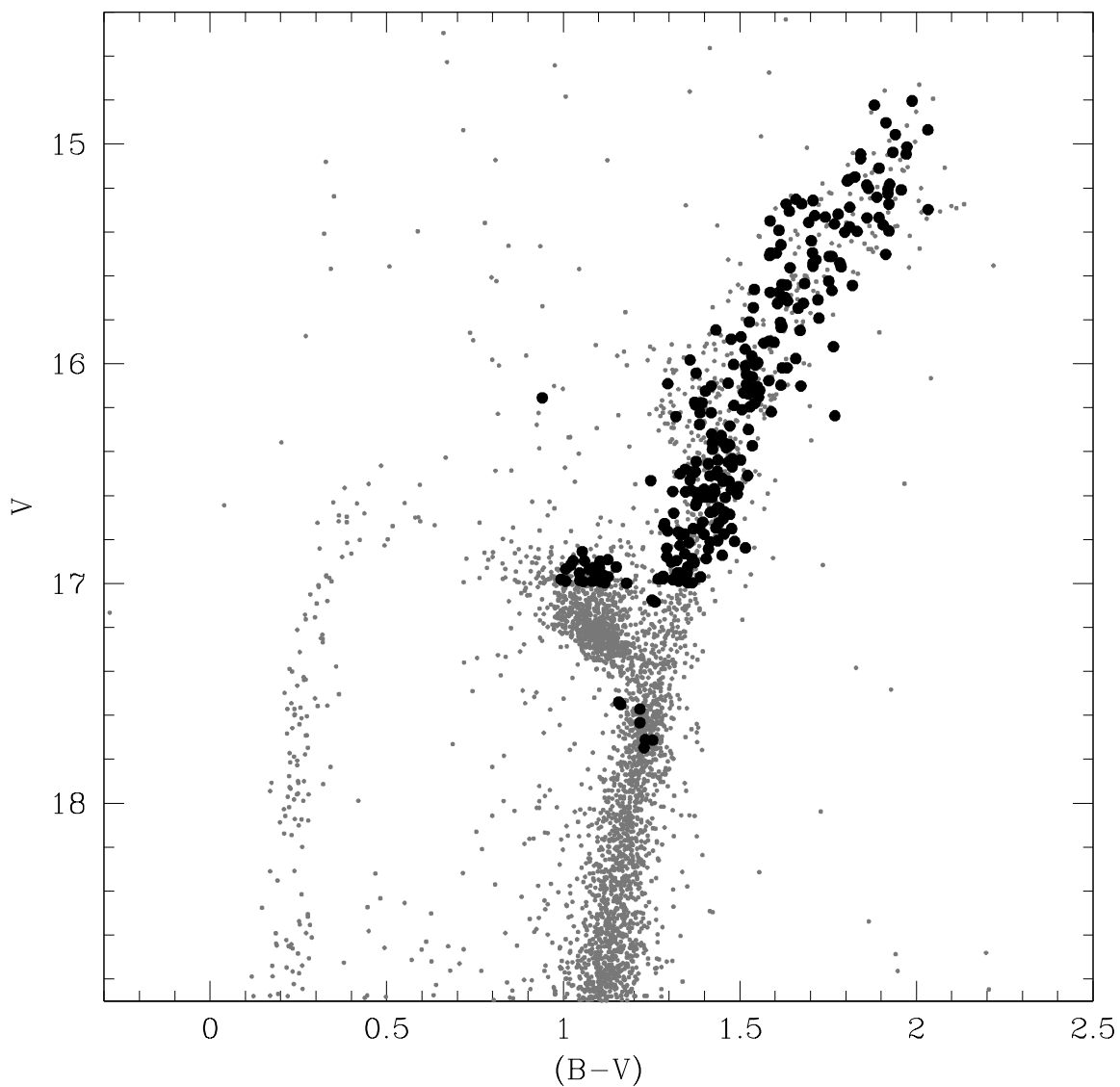


Fig. 6.— $(V, B - V)$ color-magnitude diagram of NGC 6388 obtained from HST/ACS-WFC and ESO-WFI observations (Dalessandro et al. 2008). The 276 FLAMES targets selected as cluster members are highlighted as large solid circles.

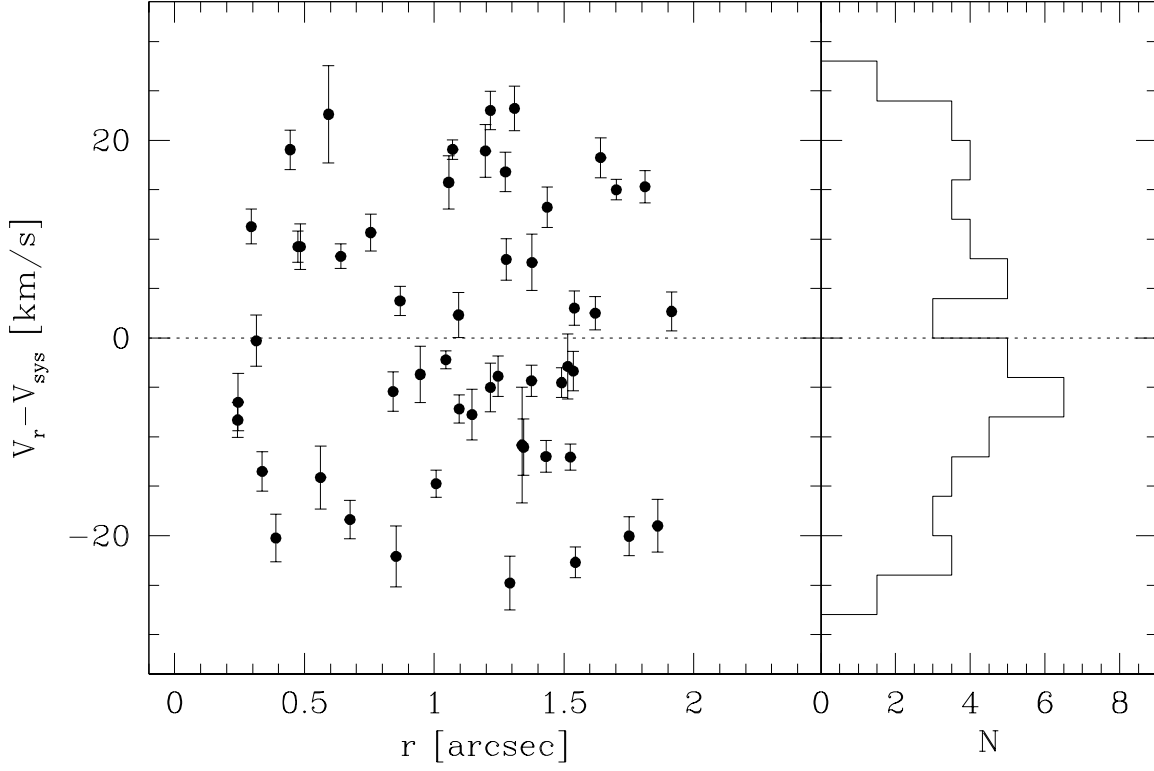


Fig. 7.— *Left panel:* Distribution of $V_r - V_{sys}$ for the 52 SINFONI targets. The histogram in the right-hand panel shows a bimodality indicating the presence of systemic rotation.

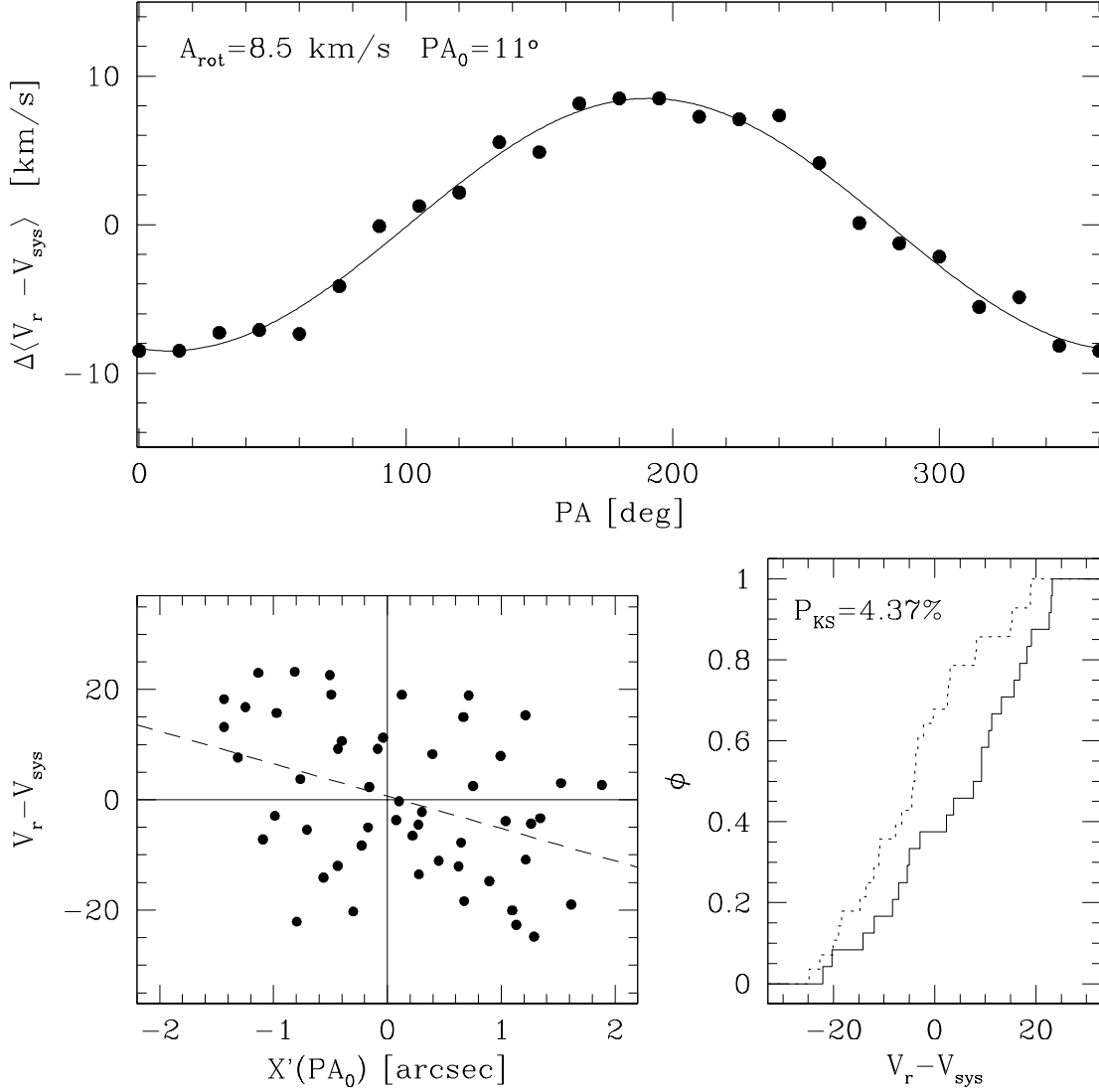


Fig. 8.— *Upper panel*: Difference between the mean radial velocities of the SINFONI targets located on each side of the cluster with respect to a line passing through the center and having position angle PA (measured from North, $PA=0^\circ$, to East, $PA=90^\circ$), as a function of PA. The solid line is the sine function that best fits the observed pattern. The corresponding values of the rotation amplitude (A_{rot}) and the position angle of the rotation axis (PA_0) are labelled. *Lower left panel*: Distribution of $V_r - V_{\text{sys}}$ as a function of the distance X' from the center projected onto the axis (dashed line) perpendicular to the best-fit rotation axis. *Lower right panel*: Cumulative radial distribution of stars having $X'(PA_0) > 0$ (solid line) and $X'(PA_0) < 0$ (dotted line). P_{KS} quotes the Kolmogorov-Smirnov probability that the two distributions are drawn from the same parent population.

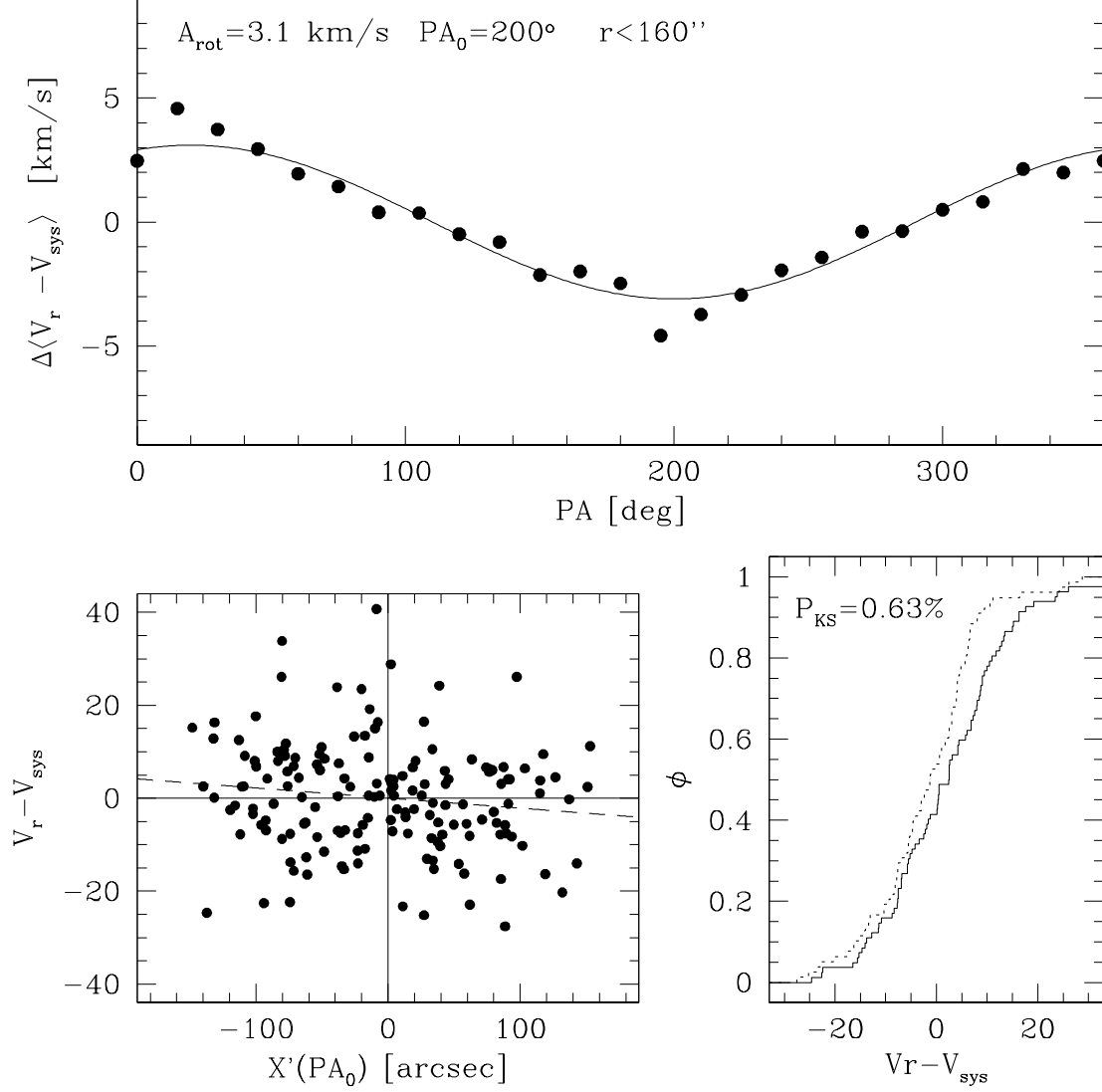


Fig. 9.— As in Fig. 8, but for the 160 FLAMES targets located between $18''$ and $160''$ from the cluster centre.

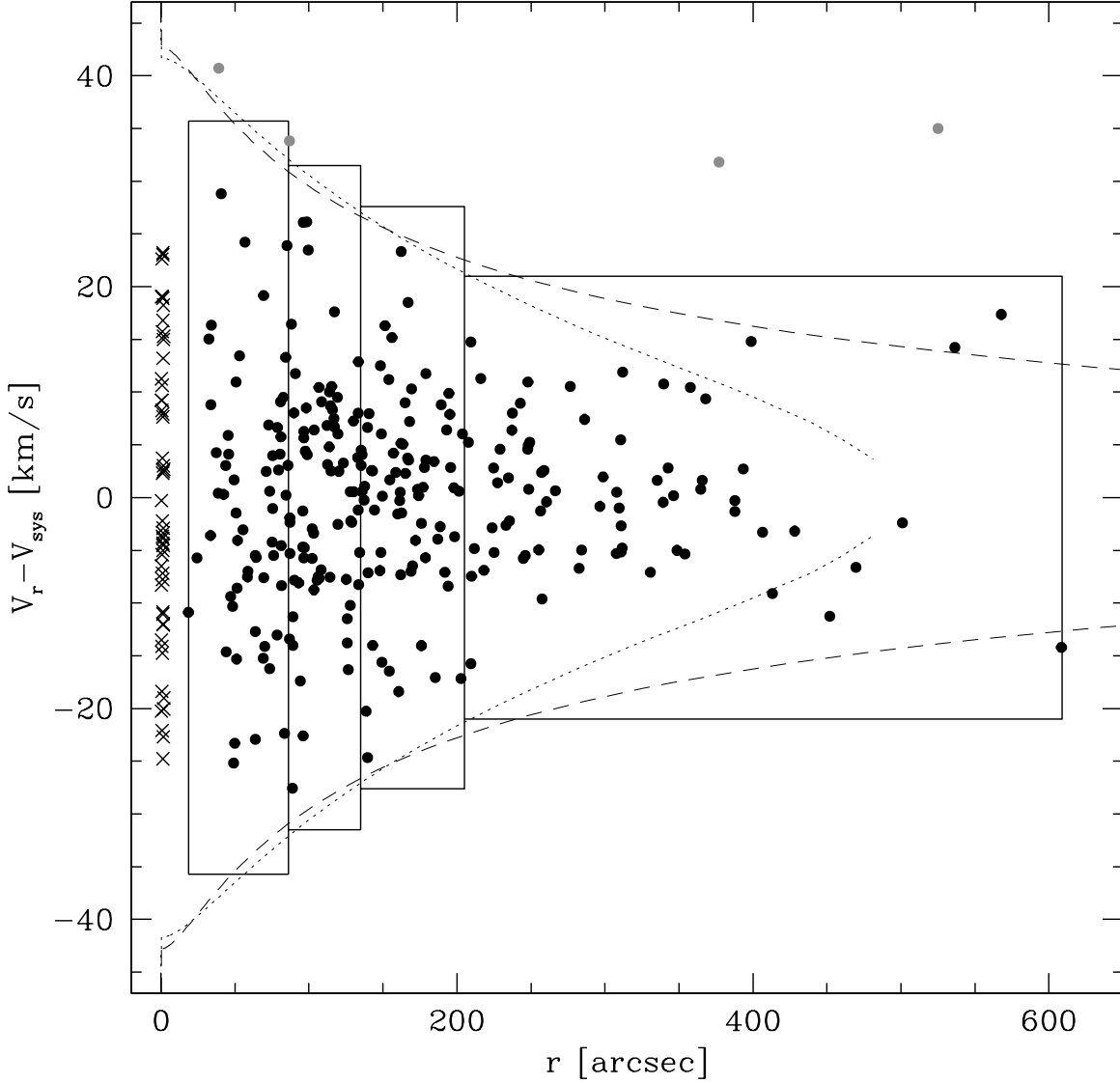


Fig. 10.— Radial velocity (referred to the cluster systemic velocity) as a function of the distance from the center, for the selected cluster members: 52 SINFONI targets are shown as crosses, 276 FLAMES stars are plotted as solid circles. The radial bins (see Table 2) adopted to determine the external portion of the velocity dispersion profile from the FLAMES data are marked as rectangles. Their vertical size corresponds to the 3σ range of the local velocity dispersion $\sigma_P(r)$; stars not included in these boxes (and not used in the computation of σ_P) are marked as grey circles. The dotted and dashed curves mark the $\pm 3\sigma$ velocity dispersion profiles of the best-fit King and Wilson models, respectively (see Sect. 4.2).

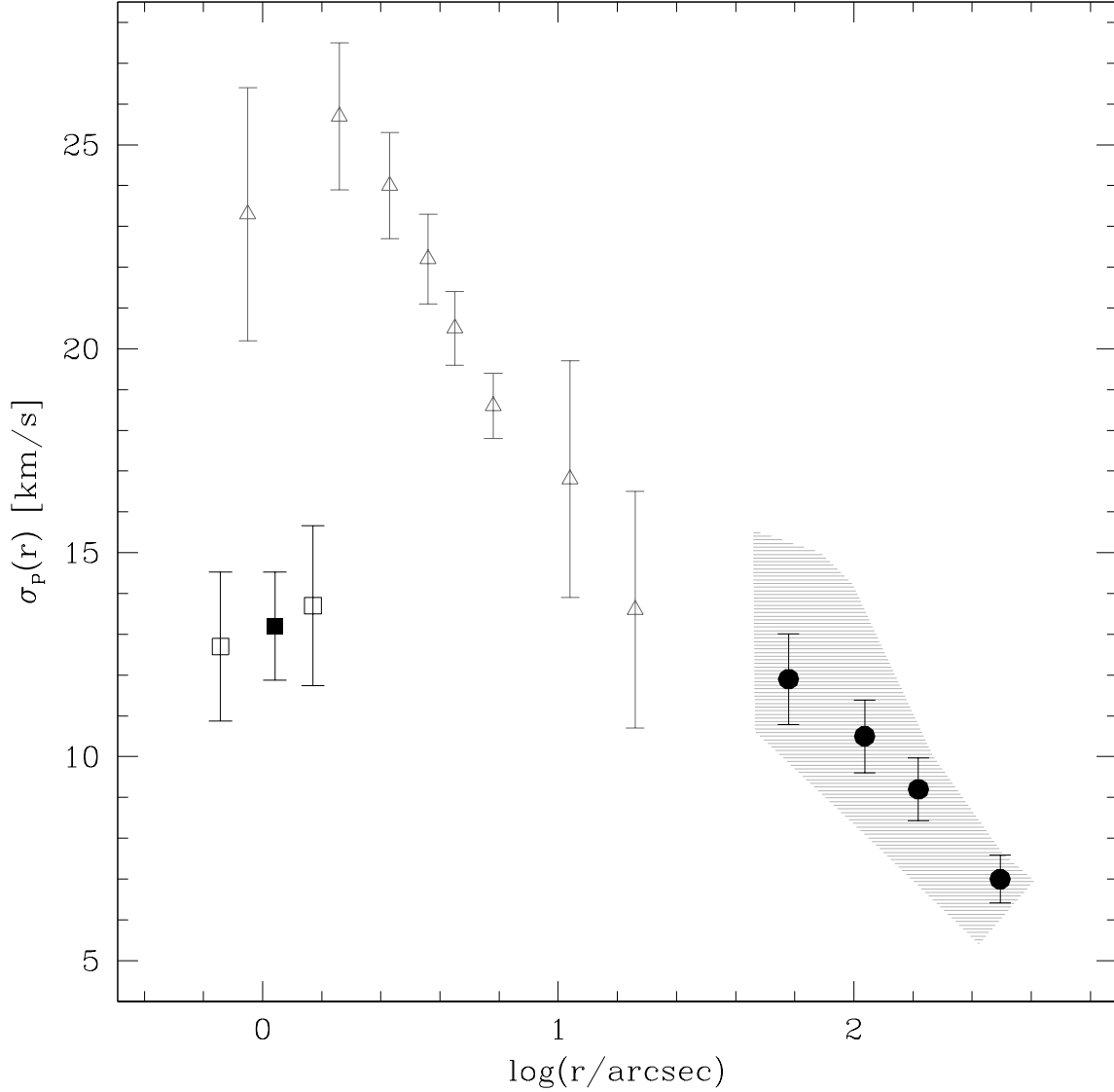


Fig. 11.— Projected velocity dispersion profile of NGC 6388 as determined from the radial velocity of individual stars (squares and circles). The solid square marks the value of σ_p obtained from the entire SINFONI sample (52 stars at $r < 1.9''$), the two empty squares correspond to the values derived within and beyond $r = 1.2''$ (26 and 26 stars in the two bins, respectively). Results from the FLAMES dataset are shown as black circles, with the grey region indicating the dispersion obtained for different choices of the radial bins. Triangles correspond to the results obtained by L11 from integrated light spectroscopy and are shown for comparison.

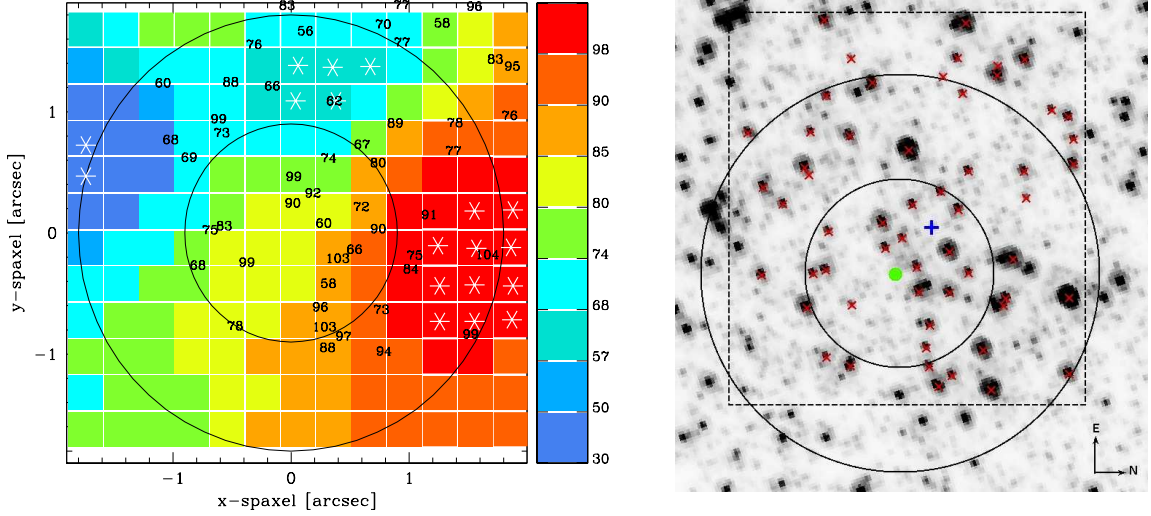


Fig. 12.— *Left panel:* Approximate reproduction of L11’s Figure 7, showing in colors their radial velocity map for the innermost $2'' \times 2''$ (North is right, East is up). The values of V_r increase from $\sim 30 \text{ km s}^{-1}$ (dark blue), to more than 100 km s^{-1} (red), as indicated in the color-bar on the right-hand side. White asterisks mark the spaxels that L11 excluded from the analysis to correct for the shot noise effect due to the presence of very bright stars. The values of the radial velocities that we measure for each individual star detected in the same field of view are marked in black at the star position. The two circles (of radius $0.9''$ and $1.9''$) correspond to the two innermost radial bins considered in L11. *Right panel:* *I*-band HST/ACS-HRC image of the same cluster region. The orientation of the map and the two circles are as in the left-hand panel, while the dashed box indicates the field of view of our SINFONI observations. Red crosses mark the stars for which we measured the radial velocity V_r , which is labelled in black in the left panel of the figure. The blue cross marks the position of the gravity centre used in the present work (from Lanzoni et al. 2007), while the green circle indicates the cluster centre adopted in L11.

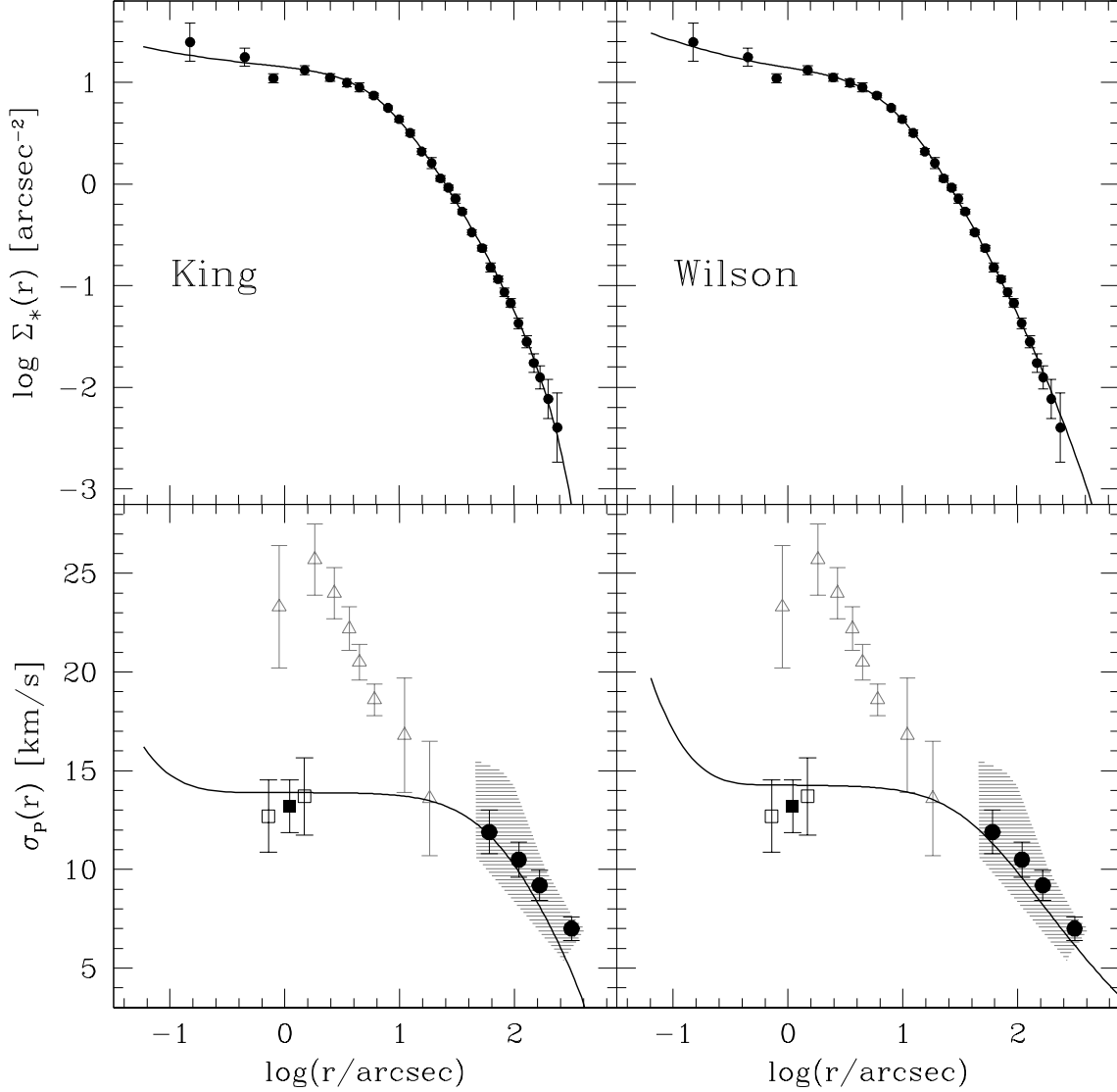


Fig. 13.— Comparison between the observations and the best-fit self-consistent King and Wilson models with central IMBH (left- and right-hand panels, respectively). The observed density profile (solid circles in the upper panels) is from Lanzoni et al. (2007). The observed velocity dispersion profile (symbols in the the lower panels) is the same as in Fig. 11. Solid lines show the best-fit model results for the mass group corresponding to $0.8 - 0.9M_{\odot}$ stars. Model parameters are given in Table 3.

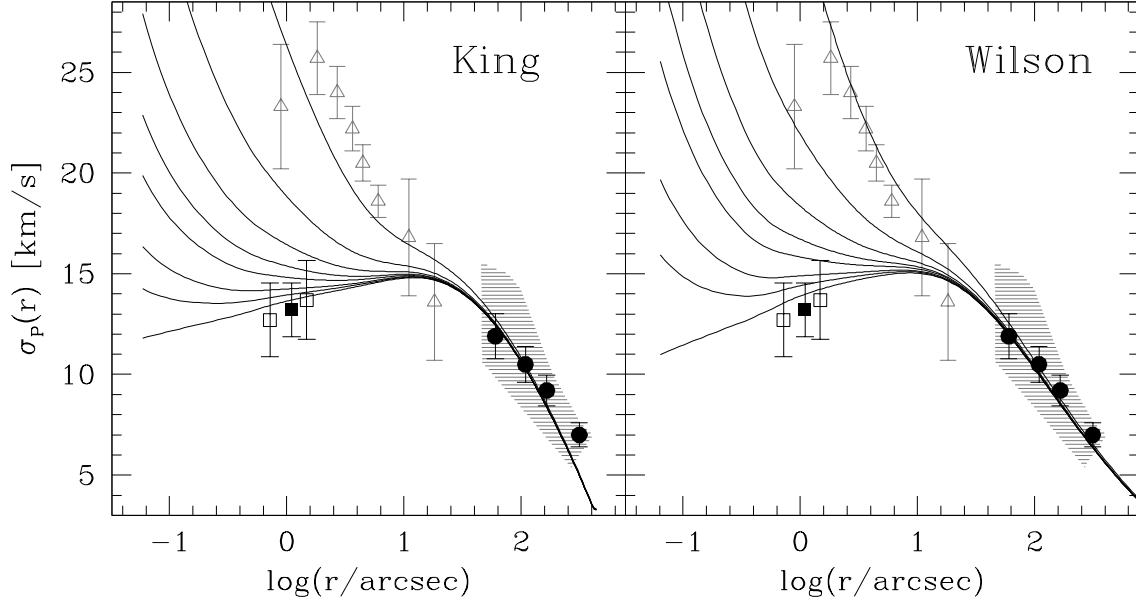


Fig. 14.— Comparison of the observed velocity dispersion profile (the same as in Fig. 11) with two families of Jeans models. *Left panel:* solid lines correspond to Jeans models calculated from the King density profile shown in the upper-left panel of Fig. 13 and by assuming different black hole masses: from bottom to top, $M_{\text{BH}}^J/M_{\text{BH}}^{\text{sc}} = 0, 0.5, 1, 2, 3, 5, 10, 30$, with $M_{\text{BH}}^{\text{sc}} = 2147M_{\odot}$. *Right panel:* the same as in the left panel, but for Jeans models calculated from the Wilson density profile shown in the upper-right panel of Fig. 13. In this case, $M_{\text{BH}}^{\text{sc}} = 2125M_{\odot}$.

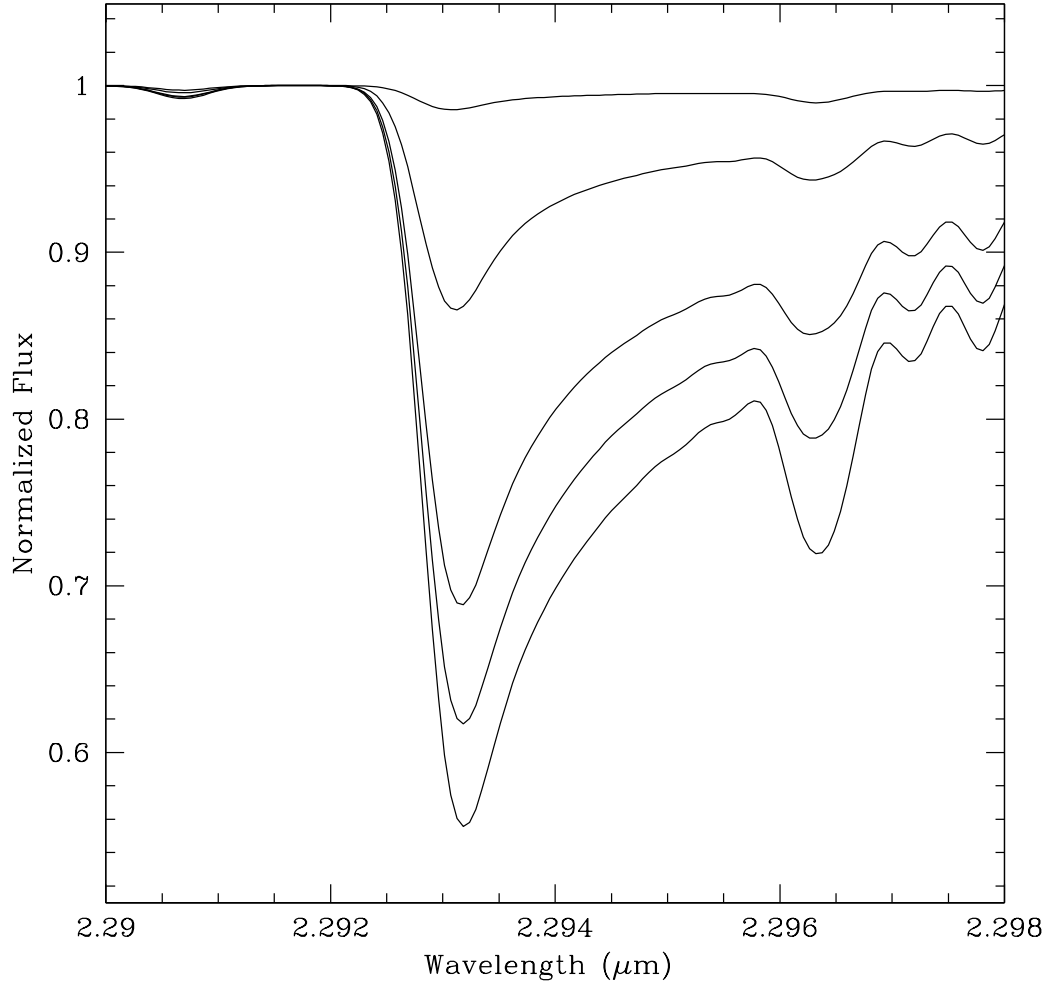


Fig. 15.— Synthetic spectra in the main CO band-head region plotted for five different values of the effective temperature (from bottom to top: $T_{\text{eff}} = 3500, 4000, 4500, 5000, 5500$ K).